

N O T I C E

THIS DOCUMENT HAS BEEN REPRODUCED FROM
MICROFICHE. ALTHOUGH IT IS RECOGNIZED THAT
CERTAIN PORTIONS ARE ILLEGIBLE, IT IS BEING RELEASED
IN THE INTEREST OF MAKING AVAILABLE AS MUCH
INFORMATION AS POSSIBLE

CK-166233
(10 copies)

ASRL TR 196-3

(NASA-CR-166233) TESTING AND EVALUATION OF
A STALL-FLUTTER-SUPPRESSION SYSTEM FOR
HELICOPTER ROTORS USING
INDIVIDUAL-BLADE-CONTROL (Massachusetts
Inst. of Tech.) 82 p HC A05/MF A01 CSCI 01C G3/08

N81-29135

Unclass
32902

TESTING AND EVALUATION OF A STALL-FLUTTER-SUPPRESSION
SYSTEM FOR HELICOPTER ROTORS USING
INDIVIDUAL-BLADE-CONTROL

by

Todd R. Quackenbush



August 1981

Distribution of this report is provided in the interest of
information exchange. Responsibility for the contents re-
sides in the author or organization that prepared it.

Prepared under research Grant No. NSG-2266 by
Aeroelastic and Structures Research Laboratory
Department of Aeronautics and Astronautics
Massachusetts Institute of Technology
Cambridge, Massachusetts 02139

for

AMES RESEARCH CENTER
NATIONAL AERONAUTICS AND SPACE ADMINISTRATION
MOFFETT FIELD, CALIFORNIA 94035

TESTING AND EVALUATION OF A STALL FLUTTER SUPPRESSION
SYSTEM FOR HELICOPTER ROTORS USING
INDIVIDUAL BLADE CONTROL

by

TODD RANDALL QUACKENBUSH

ABSTRACT

The development and testing of a feedback system designed to alleviate the violent blade first torsion mode oscillations associated with stall flutter are described. The system, based on previously developed M.I.T. Individual-Blade-Control hardware, employs blade-mounted accelerometers to sense torsional oscillations and feeds back rate information to increase the damping of the first torsion mode. A linear model of the blade and control system dynamics is developed and is used to give qualitative and quantitative guidance in the design process as well as to aid in analysis of experimental results. System performance in wind tunnel tests, both in hover and forward flight, is described, and evidence is given of the system's ability to provide substantial additional damping to stall-induced blade oscillations.

Supervisor: Dr. Norman D. Ham

Title: Professor of Aeronautics and Astronautics

ACKNOWLEDGMENTS

Though only one name appears on the cover, the success, however limited, that graced this project is due to the efforts of a number of people besides the author. Thanks are due first to Professor Norman Ham, who originated the design analyzed herein and whose many timely suggestions along the way were invaluable. Second, the generous aid and engineering expertise of Paul Bauer were crucial to this research, and his assistance allowed many knotty problems of design and implementation to be quickly resolved. Third, and most certainly not least, the author wishes to thank Bob McKillip, whose endless patience and helpfulness gave this project an essential boost, and whose previous work made the whole endeavor vastly more manageable than it otherwise would have been. Many thanks also to Ms. Marilyn Bryant for her typing of the manuscript.

TABLE OF CONTENTS

<u>Section</u>		<u>Page</u>
1	INTRODUCTION	1
2	MODEL DESIGN AND I.B.C. HARDWARE	5
	2.1 Overall Model Construction	5
	2.2 Introduction of Blade Torsional Flexibility	6
	2.3 Pitch Rate Signal Extraction	8
3	THEORETICAL ANALYSIS OF CONTROL SYSTEM	11
4	WIND TUNNEL TESTING	15
	4.1 Experimental Set-Up	15
	4.2 "Electronic Spring" Configuration Tests	15
	4.3 Tests with Mechanical Torsional Spring	19
5	CONCLUSIONS	25
	REFERENCES	26
	TABLE	27
	FIGURES	28
	APPENDICES	
1	ACCELEROMETER PLACEMENT AND SIGNAL EXTRACTION	64
2	DEVELOPMENT OF SYSTEM DYNAMIC EQUATIONS	67

LIST OF ILLUSTRATIONS

<u>Figure</u>		<u>Page</u>
1	Typical Azimuthal Angle of Attack Distribution in Forward Flight	28
2	Typical Torsion Loads on Blade Undergoing Stall Flutter	29
3	Approximation for Generalized Pitch Damping	30
4	Side View of Pitch Actuator and Blade Assembly	31
5	3/4 View of Pitch Actuator and Blade Assembly	32
6	Individual Blade Control Experimental Rig, Upstream View	32
7	Control System Block Diagram for "Electronic Spring" Tests	33
8	Detail of Blade and Accelerometer Installation, "Electronic Spring" Configuration	34
9	Detail of Blade Installation, Mechanical Spring Configuration	35
10	Integrator Frequency Response	36
11	Root Locus Diagram, "Electronic Spring" Static Test	37
12	Control System Block Diagram for Mechanical Spring Tests	38
13	Root Locus Diagrams, Static Tests with Mechanical Spring	39

LIST OF ILLUSTRATIONS (Continued)

<u>Figure</u>		<u>Page</u>
14	Root Locus Diagram, Static System with Low K_g	40
15	Open-Loop, Static "Electronic Spring" Tests	41
16	Closed-Loop, Static "Electronic Spring" Tests	42
17	Fourier Transforms of Static "Electronic Spring" Responses	43
18	Open-Loop "Electronic Spring" Tests, $\Omega = 6.2$ Hz	44
19	Closed-Loop "Electronic Spring" Tests, $\Omega = 6.2$ Hz	45
20	Fourier Transforms of "Electronic Spring" Responses, $\Omega = 6.2$ Hz	46
21	Open-Loop, Static Mechanical Spring Tests	47
22	Static Mechanical Spring Tests, Moderate Feedback	48
23	Static Mechanical Spring Tests, High Feedback	49
24	Fourier Transforms of Static Mechanical Spring Responses	50
25	Open-Loop and High Feedback Mechanical Spring Tests, $\Omega = 6.7$ Hz, $\mu = 0.0$	51
26	Open-Loop, Mechanical Spring Test, $\Omega = 6.7$ Hz, $\mu = 0.0$	52
27	High Feedback Mechanical Spring Test, $\Omega = 6.7$ Hz, $\mu = 0.0$	53

LIST OF ILLUSTRATIONS (Concluded)

<u>Figure</u>		<u>Page</u>
28	Open-Loop, Mechanical Spring Test, $\Omega = 6.7$ Hz, $\mu = 0.30$	54
29	Moderate and High Feedback Mechanical Spring Tests, $\Omega = 6.7$ Hz, $\mu = 0.30$	55
30	Open-Loop, Mechanical Spring Test, $\Omega = 6.7$ Hz, $\mu = 0.30$	56
31	Moderate Feedback, Mechanical Spring Test, $\Omega = 6.7$ Hz, $\mu = 0.30$	57
32	High Feedback, Mechanical Spring Test, $\Omega = 6.7$ Hz, $\mu = 0.30$	58
33	Low Feedback, Mechanical Spring Test, $\Omega = 6.1$ Hz, $\mu = 0.33$	59
34	Moderate and High Feedbacks, Mechanical Spring Test, $\Omega = 6.1$ Hz, $\mu = 0.33$	60
35	Low Feedback Mechanical Spring Test, $\Omega = 6.1$ Hz, $\mu = 0.33$	61
36	Moderate Feedback Mechanical Spring Test, $\Omega = 6.1$ Hz, $\mu = 0.33$	62
37	High Feedback Mechanical Spring Test, $\Omega = 6.1$ Hz, $\mu = 0.33$	63

LIST OF TABLE

<u>Table</u>		<u>Page</u>
1	Description of the Rotor Blade Used in Wind Tunnel Tests	27

LIST OF SYMBOLS

a	distance from accelerometer to blade pitch axis, m
c	blade chord, m
D_A	aerodynamic damping constant, n-m-sec
G_{OL}	open loop transfer function
K_F	control system feedback gain
K_L	control system open loop gain
K_p	feedback potentiometer gain
K_θ	servomotor pitch angle feedback gain
$K_{\dot{\theta}}$	servomotor rate feedback gain
k	reduced frequency, $\omega_\theta c/2(1-\mu)$ (.75 ΩR)
$P()$	system poles
R	blade radius, m
s	Laplace operator
V	wind tunnel speed, m/sec
β	blade flap angle rad
ζ, ζ_{eff}	effective damping ratio of blade pitch motion
θ	blade pitch angle, rad
μ	advance ratio, $V/\Omega R$
ω_θ	blade first torsion frequency, rad/sec
Ω	rotor rotational frequency, rad/sec

See Appendix 2 for further
definition of variables

SECTION 1

INTRODUCTION

As increased demands on helicopter performance have pushed machines to higher values of blade loading and advance ratio, one persistent problem for the designer has been the transient aeroelastic instability known as stall flutter. This phenomenon has been extensively studied in a variety of other works (Refs. 1-5, to name just a few) and a comprehensive discussion of its sources and effects is not necessary for present purposes. However, a brief summary of the salient points is helpful for posing the design problem dealt with herein.

It has been well documented that an airfoil oscillating rapidly in pitch is able to operate transiently at angles of attack considerably in excess of its static stall angle without flow separation taking place. However, at sufficiently high angles of attack, the airfoil stalls, though this so-called dynamic stall differs considerably from conventional static airfoil stall. As shown by Ham, Ref. 5, dynamic stall is characterized by the loss of leading edge suction and the subsequent movement of a large negative pressure disturbance aft from the leading edge, a movement which generates strong nose-down pitching moments on the airfoil. With proper combinations of airfoil mean angle of attack, amplitude of motion, and reduced frequency, this stalling phenomenon can

cause an aerodynamic moment hysteresis which can lead to a net influx of energy to the airfoil's pitching motion.

The application of these findings for airfoil dynamic stall to helicopter rotor blades is relatively straightforward. Figure 1 shows a typical azimuthal angle of attack distribution for a rotor blade in forward flight. The high angles of attack on the retreating side and the rapid pitch angle variations caused by cyclic pitch inputs strongly suggest that rotor blades under certain conditions should be susceptible to the same stall-induced oscillations observed in airfoils. Both experiments and flight experience has shown that this is indeed the case; for certain combinations of blade torsional natural frequency, blade loading, and advance ratio, the spanwise integrated effect of dynamic stall is to feed energy into blade torsional motion, particularly the first torsion mode. This motion is generally only transiently unstable and damps out rapidly as the blade swings around the azimuth toward the advancing side. However, even the one or two cycles of blade motion that do occur are sufficient to put extreme loads on the rotor control system (see Fig. 2); the fatigue life of rotor pitch links can thereby be considerably reduced.

Within the restrictions of conventional swash-plate control systems, methods to alleviate this problem all have considerable drawbacks. Increasing solidity would reduce blade loading and, thus, susceptibility to stall, but this would penalize overall

helicopter performance. Restricting the flight envelope of the machine to low advance ratios is undesirable for the same reason. Use of airfoils with more benign dynamic stall characteristics is possible, but this further complicates the already very involved rotor airfoil design process.

Applying Individual-Blade-Control (IBC) techniques to this problem offers a possible solution. Reference 6 showed that appropriate feedbacks to a position control servo governing blade pitch motion could help reduce undesirable blade motions due to low-frequency gust inputs. It was felt that similar methods could be applied to alleviate the violent torsional motions associated with stall flutter. To understand the overall concept that was employed, consider again for a moment the mechanism which drives the stall flutter oscillations. As noted previously, at high blade angles of attack and certain reduced frequencies, aerodynamic moment hysteresis causes a net input of energy to blade torsional motion, so that any small blade oscillation grows with time. Such a situation is reminiscent of simple oscillating systems operating with negative damping. Indeed, even though stall flutter of rotor blades is in reality a result of aerodynamic forcing, it can be conceived of as a phenomenon caused by a once per revolution variation in the effective damping of the blade in pitch. On the advancing side, the blade experiences strong positive damping at low angles of attack, but on the retreating side

the effective damping can temporarily become negative, leading to the oscillations described above. Figure 3 gives an idea of the variation of the effective damping function with blade operating condition.

An effective stall flutter suppression system, then, would be one which could eliminate this one-per-rev excursion into negative damping. One way to achieve this end which is suggested by classical control theory is to provide a pitch rate feedback from the blade to the pitch control servo. The details of the rationale for this concept, its implementation, and the results of experiments based on it are given in the following sections.

SECTION 2

MODEL DESIGN AND I.B.C. HARDWARE

2.1 Overall Model Construction

The model used here to test the proposed stall flutter suppression system was identical in most particulars to that used in Ref. 6. A D.C. servomotor serving, through a series of linkages, as a blade pitch position control system was mounted on the rotor shaft. The test rotor used only a single blade, with a NACA 0012 section, 21.2 inch span, and a two inch chord; further details on the blade are given in Table 1. The blade was attached to the rotor hub by means of an aluminum fork which in turn was connected to spherical bearing mounted in a ball and socket assembly; thus, the blade's flapping, lagging, and feathering motions all took place about the same point. A steel flexure instrumented with strain gauges was attached to the blade to sense pitch angle.

Two "dummy blades" in the form of lengths of threaded 5/8" steel rod were also attached to the rotor hub. Each rod had adjustable counterweights which were used to achieve dynamic balancing during rotor operation. Two symmetrically mounted counterweights were also attached to the shaft to balance the mass moment of inertia contribution of the active motor.

Photographs of the blade and control system hardware are shown in Figs. 4-6. Further details of the construction of the

actuation system are given in Ref. 6 and will not be repeated here.

2.2 Introduction of Blade Torsional Flexibility

Since the primary aim of this experiment was to design a system to control the first torsion mode of the rotor, it was necessary to ensure that the frequency of the mode was within the bandwidth of the servomotor. For full scale rotor blades, ω_θ is usually of the order of 5Ω to 7Ω , or about 30-40 Hz for most helicopters. Unfortunately, values of ω_θ for small, relatively stiff model blades such as the one employed here are invariably much higher than for full scale blades; in this case, it would have been very difficult, because of the high value of ω_θ in the test blade, to induce the blade itself to flutter. Even had that been achieved, due to restrictions on the servo bandwidth (approximately 40 Hz), control of these oscillations would have been difficult.

Given this, it was necessary to introduce torsional "softness" into the control system artificially. Two different methods to achieve this end were used here:

First, adjustment of rate and position feedbacks in the servo position control system were made to produce an "electronic spring" at the blade root. For the actuation system described in Ref. 6, the connection between the servomotor and the blade is essentially completely rigid. However, note that for this

case the transfer function of the position control system can be written as follows (neglecting pitch flexure high frequency dynamics):

$$\frac{\theta}{V} = \frac{24312.0}{s^2 + (.457 + 6953 K_\theta)s + 348200 K_\theta} \quad \begin{array}{l} \text{(See block diagram} \\ \text{in Fig. 7)} \end{array} \quad (1)$$

As is evident from the above, if K_θ were reduced to very small values, the actuator would closely resemble a very lightly damped torsional spring, with the spring's natural frequency determined by K_θ . Such a situation is a reasonable simulation of an actual rotor blade, since, for full-scale blades, most of the torsional "softness" originates in the control system itself.

Second, additional "softness" was introduced by inserting two leaves of spring steel (dimensions 3-1/2" x 1-1/8" x .02") between the blade mounting fork and blade itself (see Fig. 8). As shown in Fig. 8, the leaves were installed so that they lay parallel to the plane at the blade when at rest. This modification (which added 3.5" to the blade radius) was achieved by bolting one end of the leaves to the mounting fork which originally clamped directly onto the blade (with the aid of steel filler plates in the fork); the other ends of the leaves were secured to the blade with the aid of two 2-1/4" x 1-1/4" x 3/16" aluminum clamping plates built for this purpose (steel

fillers were again used between the clamping plates). Details of the "tuning" of this arrangement to give the desired ω_0 are given in Section 4.

2.3 Pitch Rate Signal Extraction

As noted in Section 1, the principal aim of this experiment was to increase the damping of blade torsional oscillations by supplying a pitch rate feedback to the position control system. It was decided to extract the pitch rate signal by first obtaining a pure pitch acceleration signal from accelerometers mounted on the blade and then feeding this signal to an integrator.

Appendix 1 discusses in detail the signals sensed by accelerometers mounted a distance a away from the pitching axis of the blade. As noted in that Appendix, any single accelerometer mounted away from the pitching axis will sense a component of centrifugal force (often called "propeller moment") which is proportional to pitch angle. This difficulty can be overcome if the signals from two separate accelerometers mounted of an equal distance from the pitching axis but oriented with a 90° separation between them are summed; the result is a signal purely proportional to $\ddot{\theta}$.

Unfortunately, the above result is strictly true only if the flapping and lagging degrees of freedom are neglected. Unless the accelerometers are placed such that they lie in the plane formed by the lagging and flapping axes, components of

centrifugal force proportional to lag angle ζ and flap angle β will enter into the signal sensed by the accelerometers. This situation has the potential for causing difficulties with the integrated feedback signal, since an ideal integrator would apply an infinite d.c. gain to any steady-state components in the ζ and β signals. Fortunately, the actual integrator used here was non-ideal, having a roll-off at low frequencies (below approximately 0.5 Hz) (see Fig. 10) which would eliminate any steady-state signals. However, blade lag motion characteristically also involves a low frequency component at approximately 0.2 Ω to 0.4 Ω ; to minimize the possibility that the integrator would amplify these low frequency signals (at approximately 1.3 to 2.6 Hz for the rotor speeds used here) and distort the feedback, the brackets holding the accelerometers were built such that they were rigidly attached to the blade but were located in the plane of the lagging and flapping axes (see Fig. 9). These brackets were sized to be used with the "electronic spring" blade configuration i.e., when the spring steel inserts were not present between the actuator fork and the blade. When these inserts were used, it became impracticable to have the accelerometers lie in the plane of the flapping and lagging axes; the same accelerometer brackets shown in Fig. 8 were used in this case without apparent adverse effect on system performance.

The accelerometer installation shown in Fig. 3 will inevitably sense a strong $l\Omega$ signal if a pilot pitch input (cyclic) is used. This circumstance will not interfere with the intended purpose of this feedback control system (i.e., providing additional damping to transient disturbances in torsion) since the $l\Omega$ is a steady input; a rate feedback on such a signal will merely introduce a phase lag which can be compensated for elsewhere in the pitch control system.

SECTION 3

THEORETICAL ANALYSIS OF CONTROL SYSTEM

To see the fundamental concept behind the flutter alleviation system studied here, first note the system block diagram in Fig. 7. This diagram illustrates the "electronic spring" case, in which torsional softness is obtained by reducing K_{θ} to low values and then adjusting K_{θ} to obtain the desired "spring" undamped natural frequency. The open loop transfer function of this system for $\Omega = 0$ is given by

$$G_{ol} = \frac{.298 K_F s^3}{(1 - \frac{s}{p_1})(1 - \frac{s}{p_2})(1 - \frac{s}{p_3})(1 - \frac{s}{p_4})(1 + \frac{s}{s_o})^2} \quad (2)$$

$$p_1 = -182.7 + 416.0j \quad p_2 = -164.2 + 328.5j$$

The above poles p_1 and p_2 are obtained from Fig. 7 for $K_{\theta} = .234$ and $K_{\theta} = .05$, with the pitch flexure dynamics included. As the root locus diagram (Fig. 11) shows, the inclusion of the pitch flexure dynamics (discussed in Appendix 2) considerably changes the simple system model one would have expected were these dynamics neglected, as they were in Eq. 1. However, Fig. 11 also shows that the feedback nevertheless achieves the fundamental aim, i.e., increasing the damping of the blade "first torsion mode". It is clear, though, that the range of

permissible K_F values is limited, since large K_F drives the flexure pole unstable.

For the case in which flexible leaves are inserted between the actuator fork and the blade, the dynamics of the system become somewhat more involved, since in this case the blade pitch angle can differ from the motor shaft command pitch angle, unlike the earlier case in which the shaft/blade connection was essentially rigid. The changes effected in the system equations of motion and in the overall system dynamics by this additional degree of freedom are shown in detail in Appendix 2. For this case, the effect of including the pitch flexure dynamics was negligible. The open loop transfer function for the "mechanical spring" system for $\Omega = 0$ is then

$$G_{ol} = \frac{.127 K_F s^3}{\left(\frac{s}{160.6} + 1\right) \left(\frac{s}{127.0} + 1\right) \left(1 - \frac{s}{p_1}\right) \left(1 - \frac{s}{p_2}\right) \left(1 + \frac{s}{z_0}\right)} \quad (3)$$

$$K_\theta = .528 \quad K_{\dot{\theta}} = .19 \quad p_1 = -2.75 + 192.9j$$

The block diagram of the system is shown in Fig. 12 and the root locus diagram is shown in Fig. 13 for $K_\theta = .528$ and $K_{\dot{\theta}} = .19$. These values of K_θ and $K_{\dot{\theta}}$ were chosen since they gave what appeared to be an acceptably large range of values in which the rate feedback could succeed in keeping the blade oscillations stable; different values of feedback gain, for example $K_\theta = .528$, $K_{\dot{\theta}} = .08$, would produce a root locus

diagram such as in Fig. 14, in which any but very small values of K_F drive the blade oscillations unstable.

Note that the system dynamics detailed above neglect the effects of aerodynamic damping (be it positive or negative) on the blade. Inserting a term $D_A \dot{\theta}$ in the equations of motion of Appendix 2 to account crudely for aerodynamic damping shows that the effect of aerodynamics is to move the blade oscillation pole of Fig. 13 to the right with negative D_A , while oscillation frequency is nearly constant; for sufficiently large, negative values of D_A the pole is driven into the right half-plane, but only transiently, since D_A and, thus, pole location vary with azimuth. For proper choices of K_θ and K_F though, blade oscillations can be stable all around the azimuth (again see Fig. 13); nor should the value of K_F required to stabilize the pitch oscillations be excessive, since the effective "negative damping ratios" associated with stall-induced instabilities are rather small ($\zeta_{\text{eff}} \approx -0.1$ at a maximum).

Figure 13 illustrates two interesting aspects of the model developed here. First, the root locus diagram indicates that the blade oscillation frequency will increase substantially as K_F is increased. Second, the analysis predicts that the oscillation will be stabilized for only a certain range of K_F values and will develop a relatively high-frequency, potentially unstable oscillation if K_F is increased sufficiently. As will be discussed in Section 4, both qualitative and quantitative

agreement was found between the predictions made above (and in Appendix 2) and actual experimental results.

Finally, as is evident from the above discussion, little in the way of detailed aerodynamic or structural analysis was done preparatory to the experiments described herein; this circumstance came about fundamentally because it was felt that such analysis was impracticable and unnecessary given the intended scope of the present work. A number of detailed and complex analyses of stall flutter and its effects on rotor blades have already been performed with powerful computational tools and elaborate models (see, for example, Refs. 7,8). It was felt that since the system to be designed and tested here was to be a first-pass, proof-of-concept effort, the simple dynamic and aerodynamic models used above and in Appendix 2 were adequate to the task. This evaluation was borne out by the results presented in Section 4.

SECTION 4

WIND TUNNEL TESTING

4.1 Experimental Set-Up

Testing of the I.B.C. stall flutter suppression system was performed in the M.I.T. Wright Brothers Wind Tunnel. The 7' x 10' test section contained two vertical trunnions which supported the rotor shaft in a horizontal attitude. This orientation, which caused the rotor to rotate in a vertical plane, was a result of the mounting requirements of the previous series of I.B.C. gust alleviation tests (Ref. 6). One consequence of this orientation was to introduce a one-per-rev gravity pulse into the accelerometers used in the control system; however, the magnitude of the pulses was sufficiently small that no adverse effect on system performance was expected or observed.

The rotor was driven by an external hydraulic motor. The shaft was equipped with slip rings to provide power to the servomotor and to extract data from the various sensing elements. On-line data extraction was accomplished using software previously developed by other members of the I.B.C. project team.

4.2 "Electronic Spring" Configuration Tests

The first series of tests involved four experiments using the "electronic spring" configuration. For those tests, as noted in Section 2, a rigid motor shaft-blade linkage was used,

and torsional softness was introduced by adjusting rate and position feedbacks in the servo (see Fig. 7). For the values chosen ($K_{\theta} = .234$, $K_{\dot{\theta}} = .05$), the effective damped natural frequency of the blade in pitch was 53 Hz.

First, two static tests were conducted with the blade hanging vertically downward. A pulsed voltage signal was fed into the pitch control system to excite blade motion. The signal consisted of a series of 4.0 ms pulses at 6.0 Hz with an amplitude of 0.75 volts (equivalent to 3° of pitch). Blade pitch rate and acceleration response to this input for the open loop case are shown in Fig. 15. Next, the control loop was closed by applying the pitch rate feedback to the servomotor input; the potentiometer setting K_p in the feedback loop was 0.54. For the same excitation as the previous case, the pitch rate and acceleration traces shown in Fig. 16 were obtained. Comparing the time traces in Figs. 15 and 16, one can see that the damping of the rate response for the closed loop case is higher than that in the open loop case; the effective damping ratio for the latter is 0.13, as opposed to 0.23 for the former. Note that the closed loop case response contains a substantial high-frequency component that is not evident in the open loop trace; this is the pitch flexure mode, which moves to lower damping and higher frequency as K_p is increased (see Fig. 11). The amplification at this high frequency component is not desirable nor, though, is it material to the current aim of

adding damping to the blade "first torsion" mode. As Fig. 17 (which gives the Fast Fourier Transforms of the rate responses for the open and closed loop cases) shows, blade response to the pulsed input has been substantially decreased in the vicinity of the original "first torsion" frequency of 53 Hz.

A similar experiment was then performed with the same K_0 , K_0 and input excitation, however, in this case the rotor was spun at 6.2 Hz; the aim here was to ensure that the control system would operate properly with a non-zero propeller moment being sensed by the accelerometers. Spinning the rotor had no apparent adverse effects on system performance in this configuration, and a comparison of rate and acceleration traces as well as the Fourier-transformed rate responses for the open and closed loop cases is shown in Figs. 18, 19 and 20. Here, the closed-loop pitch rate response has an effective damping ratio of 0.25, as opposed to 0.18 for the open loop case. Note also that the effective damped natural frequency of the rotating open loop case appears, from Fig. 20, to be approximately 47 Hz, as opposed to 53 Hz for the non-rotating case. This is not surprising, since rotor rotation causes aerodynamic damping to be added to the blade/servo system, driving the blade pole of Fig. 11 farther into the left half-plane, which leads to a lower damped natural frequency, given the pole's trajectory. Despite this difference, substantial reductions in blade rate response around the "first torsion" frequency were observed, just as in the non-rotating case.

Though these experiments were not realistic in the sense that they relied on electronic rather than aerodynamic excitation, and in the sense that the dynamics of the "electronic spring" used here only vaguely resembled those of a real rotor blade, nevertheless they demonstrated that the proposed control system had the ability to increase the damping of high frequency (approx. 50 Hz) oscillations in pitch (equivalent to oscillations in torsion for this simple dynamic system). Furthermore, these results had considerable qualitative and quantitative agreement with the theoretical predictions of Appendix 2 and thus gave some grounds for confidence in the analytical methods used. For example, for the non-rotating case, Appendix 2 predicts damped natural frequencies of 52 Hz and 66 Hz for the blade and flexure oscillation modes, respectively, for the open loop case; the values obtained from experiment were 53 and 71 Hz, respectively.

Unfortunately, it was also found that the blade in the "electronic spring" configuration was not easily susceptible to stall flutter, despite vigorous attempts to excite the blade both in hover and in forward flight. The determination was therefore made to switch to the mechanical spring configuration described in Section 2. Previous tests at the M.I.T. VTOL Technology Lab had shown that this configuration was susceptible to stall flutter.

4.3 Tests with Mechanical Torsional Spring

After the installation of the mechanical spring described previously, a series of tests were run with the blade static, in hover, and in forward flight at two separate advance ratios. The static tests were designed to reestablish the fundamental workability of the proposed control system given the substantial change in system dynamics introduced by the mechanical spring. Before these tests were conducted, a choice had to be made concerning the number of steel leaves to be inserted between the actuator and the blade, since the number of leaves determines natural frequency of the torsional spring. One leaf (installed as shown in Fig. 9) yielded an ω_0 of approximately 17 Hz, while two leaves yielded 31 Hz, and three leaves 42 Hz. The two-leaf configuration was chosen since the frequency fell within the bandwidth of the servo and also provided sufficient flapwise stiffness to avoid interference between the blade and the shaft support trunnions during rotor run-up.

The static tests proceeded much as did those with the electronic spring configuration; the blade was hung vertically downward from the shaft while an external pulse train of frequency 6.7 Hz was introduced to excite blade motion. For these tests, and for all succeeding tests, three separate levels of K_p (0.0, 0.13, and 0.26) were established as benchmarks which covered the significant range of system performance and which would be used as operating points in those cases

where circumstances permitted. The rate and acceleration responses of the blade to the identical pulse input for these three levels of K_p are shown in Figs. 21, 22, and 23. Graphic representations of the Fast Fourier Transform of the pitch rate signals for $K_p = 0.0$ and $K_p = .26$ are shown in Fig. 24. Both of these sets of results reflect the trends predicted in Section 3; the damping of the blade oscillations of the blade "first torsion" node is increased with increasing K_p , while the frequency of the oscillation increases. Note that the values of K_p used here correspond to the indicated points on the root locus diagram of Fig. 13.

The values of K_p are multiplied by the appropriate constants (see Fig. 12) to yield the total feedback gain K_F . The overall open-loop gain K_L which is used in generating Fig. 13 is obtained by multiplying K_F by the forward loop gain of .127 (see Appendix 2). The values of K_L corresponding to $K_p = .13$ and $K_p = .26$ are, respectively, .000135 and .00027. As seen from Fig. 13, these values of K_L correspond to blade oscillations with $\zeta = .06$ and damped natural frequency of 208 rad/sec (for $K_p = .13$) and $\zeta = .085$ and damped natural frequency of 224 rad/sec (for $K_p = .26$). These values can be compared to values of .15 and 212 rad/sec, respectively, for $K_p = .13$, and .24 and 233 rad/sec, respectively for $K_p = .26$, that were observed experimentally. These results suggest that there was considerably more damping present in the system than the model

of Appendix 2 assumed. This is not too surprising, since only the mechanical friction of the motor itself was included in the model; many other possible sources of friction (e.g. gear meshing, linkage friction) doubtless existed but were difficult to include in a linear model and so were neglected. The relatively close agreement of the frequency predictions, though, was encouraging, as was the fact that the model predicts that the system will go unstable at high gain at 70 Hz, which agreed reasonably closely with the 65 Hz observed in experiments.

Unfortunately, the usefulness of the model in Appendix 2 is limited to the static rotor cases. The time-varying aerodynamic damping in the hover and forward flight cases introduces sufficient additional complications that detailed predictions with this model, which neglects aerodynamic effects, become invalid. However, as will become apparent in the following discussion, the overall functioning of the system is not impaired by this circumstance.

To summarize, then, the effective damping ratio of the $K_p = 0.0$ case was .02, while for $K_p = .13$ it was .15, and for $K_p = .26$ it was .24. From Fig. 24, one also notes that the pitch rate component at ω_θ was decreased dramatically relative to the $K_p = 0.0$ case with $K_p = .26$. These results again show the strong potential of this system for increasing the damping of torsional oscillations in the 30-40 Hz frequency range.

The next step in testing was to run three cases with the rotor operating in hover and with external pitch excitation supplied. Ordinarily, it is possible (see Ref. 5) to induce stall flutter in hover by raising collective pitch until the blade stalls and provides the necessary excitation. However, the pitch linkage on the model rotor had not been specifically designed to operate at high collective, and the maximum settings available (16° - 17°) were insufficient for the deep blade stall needed, so once again resort was made to external excitation.

For these hover tests, the rotor was operated at 15° collective in order that aerodynamic damping would be low. (see Fig. 3). Rotor rotation frequency was 6.7 Hz, and the frequency of external excitation was either 6.7 Hz or 3.4 Hz, while the magnitude of each input pulse varied from case to case (though it was never more than approximately 2° or 0.63 volts). A comparison of the pitch rate responses for $K_p = 0.0$ and for $K_p = 0.26$ are shown in Fig. 25. (Note that excitation frequency was only 3.4 Hz for $K_p = 0.0$; given the low aerodynamic damping, any more strenuous excitation might have generated a divergent oscillation.) The effective damping ratio for the $K_p = 0.0$ is 0.03, while for $K_p = .26$ it is 0.14. A comparison of the FFT breakdowns of the pitch acceleration response for the two cases in Figs. 26 and 27 shows once again the large decreases in acceleration components in the vicinity of $\omega_0 = 31$ Hz. Also evident when K_p is increased, though, is an amplification of

pitch acceleration response at frequencies higher than ω_θ (at approximately 40 Hz or about 6Ω). One possibility is that this shift is a result of the "stiffening" effect predicted in Section 3 and noted in the description of the non-rotating tests above i.e. that increases in K_p tend to cause ω_θ itself to increase. However, such inferences are complicated by the fact that significant aerodynamic damping is present in the rotating tests and, as noted previously, such effects can also alter the blade oscillation frequency. Hence, in the absence of a detailed aerodynamic model, it is difficult to isolate the cause of this frequency shift. Nevertheless, the overall aim of demonstrating that high frequency oscillations could be suppressed was achieved.

To complete the testing series, two sets of forward flight cases at moderate advance ratio were run. In these cases it was found that stall flutter could be brought about and, thus, resort did not have to be made to external pitch excitation. For the first set of runs, rotation frequency was 6.7 Hz, tunnel speed was 20 mph, and hence advance ratio was 0.30. As shown in the top of Fig. 28, root collective pitch was 10° and a one-per-rev cyclic pitch signal of $\pm 9.0^\circ$ was superimposed, with the maximum pitch angle reached at $\psi = 270^\circ$. The lower trace of Fig. 28 shows the pitch rate response of the blade; superimposed on the strong one per rev is the higher frequency oscillation caused by dynamic stall, which shows up as the slight "lumpiness" in the pitch rate curve. The effect is also evident in the pitch acceleration response in Fig. 30.

The effect of increasing K_p from zero is shown in Figs. 29, 31, and 32. With progressively higher values of K_p , the "lumpiness" of the pitch rate curves smooths out, representing a diminuation of the stall-induced oscillations. The acceleration response reflects the same trends, with the high frequency oscillations decreasing in magnitude; the FFTs of the pitch acceleration response shows that $K_p = .13$ causes a reduction of approximately 33% in the component at ω_θ over the $K_p = 0.0$ case, while $K_p = .26$ leads to a reduction of approximately 67%.

A second set of forward flight experiments was performed at essentially the same collective, cyclic, and wind speed settings, though the advance ratio was increased to 0.33 by decreasing Ω to 6.1 Hz. This flight condition induced a substantially stronger stall flutter oscillation than in the previous case, so much so that, as seen in Fig. 33, K_p could not be reduced to zero, only to .02, lest a violent oscillation develop. Even with this stronger excitation, though, settings of $K_p = .13$ and .26 were sufficient to damp out the torsional oscillations to a substantial degree (see Figs. 34-37). It is interesting to note that most of the beneficial effect of the feedback is obtained with $K_p = .13$; increasing K_p to .26 produces only a marginal further improvement.

SECTION 5
CONCLUSIONS

From the preceding calculations and experiments, the following conclusions can be drawn:

1. Treating stall flutter as a phenomenon induced by time-varying aerodynamic damping serves as an effective point of departure for analysis and design of a stall flutter suppression system.
2. A relatively simple linear model of the blade and servomotor dynamics can serve to give substantial quantitative and qualitative guidance as to feedback gain selection for a stall flutter suppression system based on I.B.C. techniques.
3. A system centered around the concept of providing rate feedback to the blade control motor from blade-mounted accelerometers can generate increased damping of first torsion oscillations induced by either externally imposed or aerodynamic excitation.
4. No apparent fundamental obstacle exists to extending the control techniques developed herein to larger scale systems.

REFERENCES

1. Carta, F.O. and Niebanck, C.F., "Prediction of Rotor Instabilities at High Forward Speeds", Vol. III: Stall Flutter, USAAVLABS TR 68-18C, Feb. 1969.
2. Arcidiacono, P.J., Carta, F.O., Cassellini, L.M. and Elman, H.L., "Investigation of Helicopter Control Loads Induced by Stall Flutter", USAAVLABS TR-70-2, Mar. 1970.
3. Carta, F.O., Commerford, G.L., Carlson, R.G. and Bladewell, R.H., "Investigation of Airfoil Dynamic Stall and Its Influence on Helicopter Control Loads", USAAMRDL TR-72-51, Mar. 1970.
4. Ericcson, L.E. and Reding, J.P., "Dynamic Stall of Helicopter Blades", Journal of the American Helicopter Society, pp. 11-19, Jan. 1972.
5. Ham, N.D. and Young, M.I., "Torsional Oscillation of Helicopter Blades Due to Stall", Journal of Aircraft, pp. 218-224, May-June 1966.
6. McKillip, R.M., "The Design, Testing, and Evaluation of the M.I.T. Individual Blade Control System as Applied to Gust Alleviation for Helicopters", ASRL TR 196-1, Dept. of Aeronautics and Astronautics, M.I.T., Feb. 1980.
7. Tarzanin, F.J. and Ranieri, J., "Investigation of the Effect of Torsional Natural Frequency on Stall Induced Dynamic Loading", USAAMRDL TR 73-94, Feb. 1974.
8. Ham, N.D., "Aerodynamic Loading on a Two-Dimensional Airfoil During Dynamic Stall", AIAA Journal, 6, 10, pp. 1927-1934, Oct. 1968.

TABLE 1
DESCRIPTION OF THE ROTOR BLADE USED
IN WIND TUNNEL TESTS

No. of blades	1
Radius, w/o steel leaves	2.03 ft.
Radius w/ steel leaves	2.311 ft.
Chord	2.0 in.
Section	NACA 0012
Lift-Curve Slope	5.73
Drag Coefficient	.012
Rotational Speeds, Forward	{ 6.7 Hz (first test)
Flight Cases	
Aerodynamic Center	25% chord
Hinge Offset	2.0 in.
Built-in Angle of Twist	8 deg. (linear)

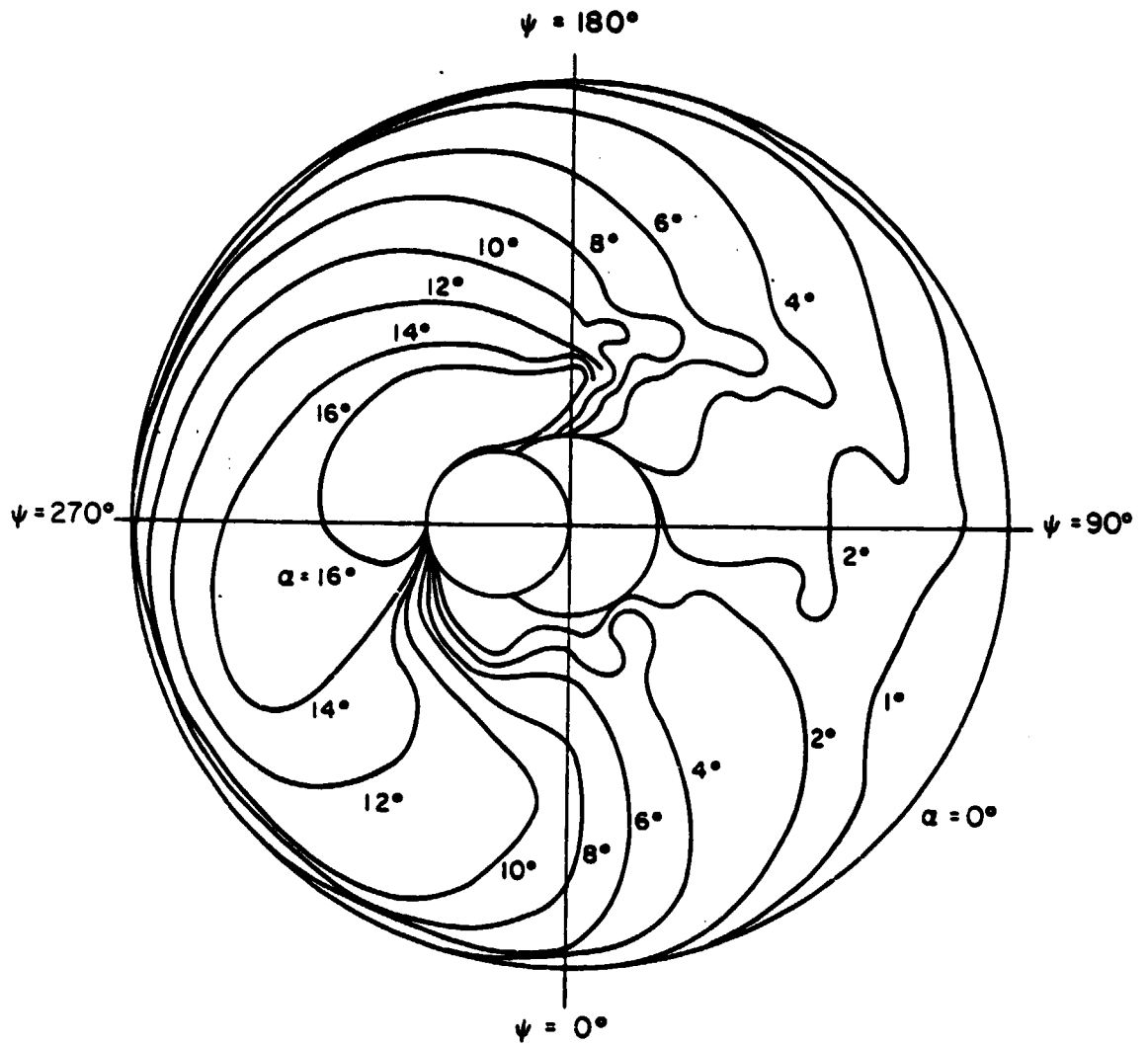


FIG. 1 Typical Azimuthal Angle of Attack Distribution in Forward Flight

$$C_{T/\sigma} \approx .111$$

$$\mu \approx .17$$

ABSOLUTE PRESSURE
TRANSDUCER LOCATED
AT 5% CHORD
80% RADIUS

PITCH LINK LOAD

TORSION STRAIN
AT 13% RADIUS

TORSION STRAIN
AT 46% RADIUS

TORSION STRAIN
AT 69% RADIUS

TORSION STRAIN
AT 90% RADIUS

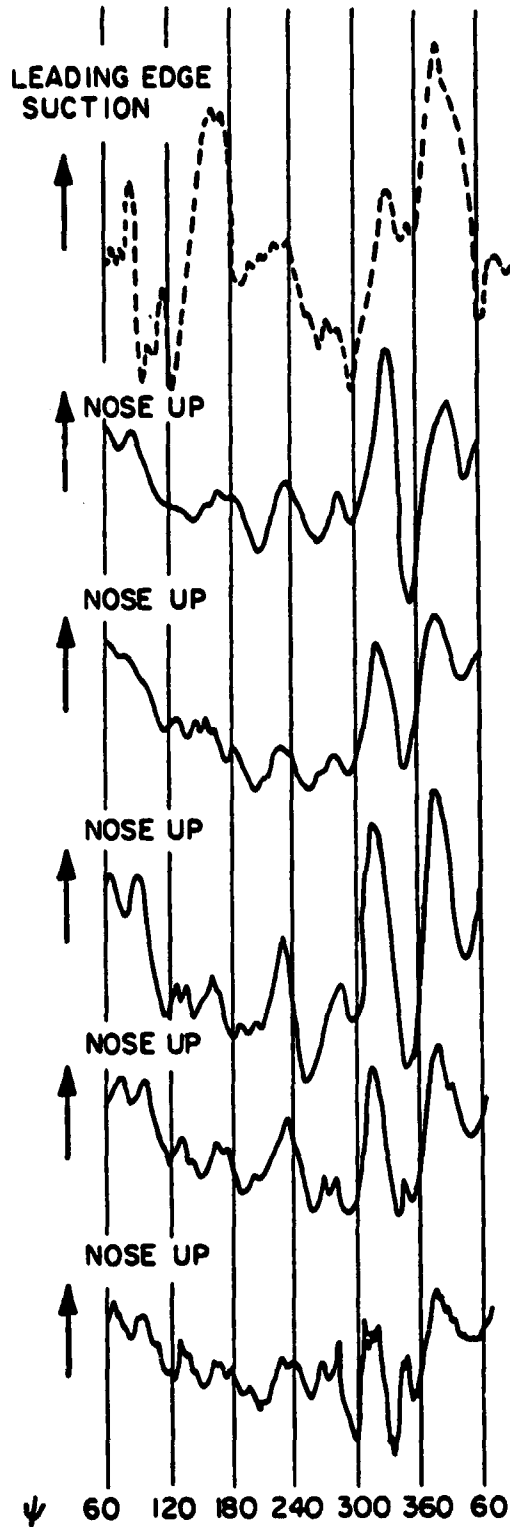


FIG. 2 Typical Torsion Loads on Blade Undergoing Stall Flutter

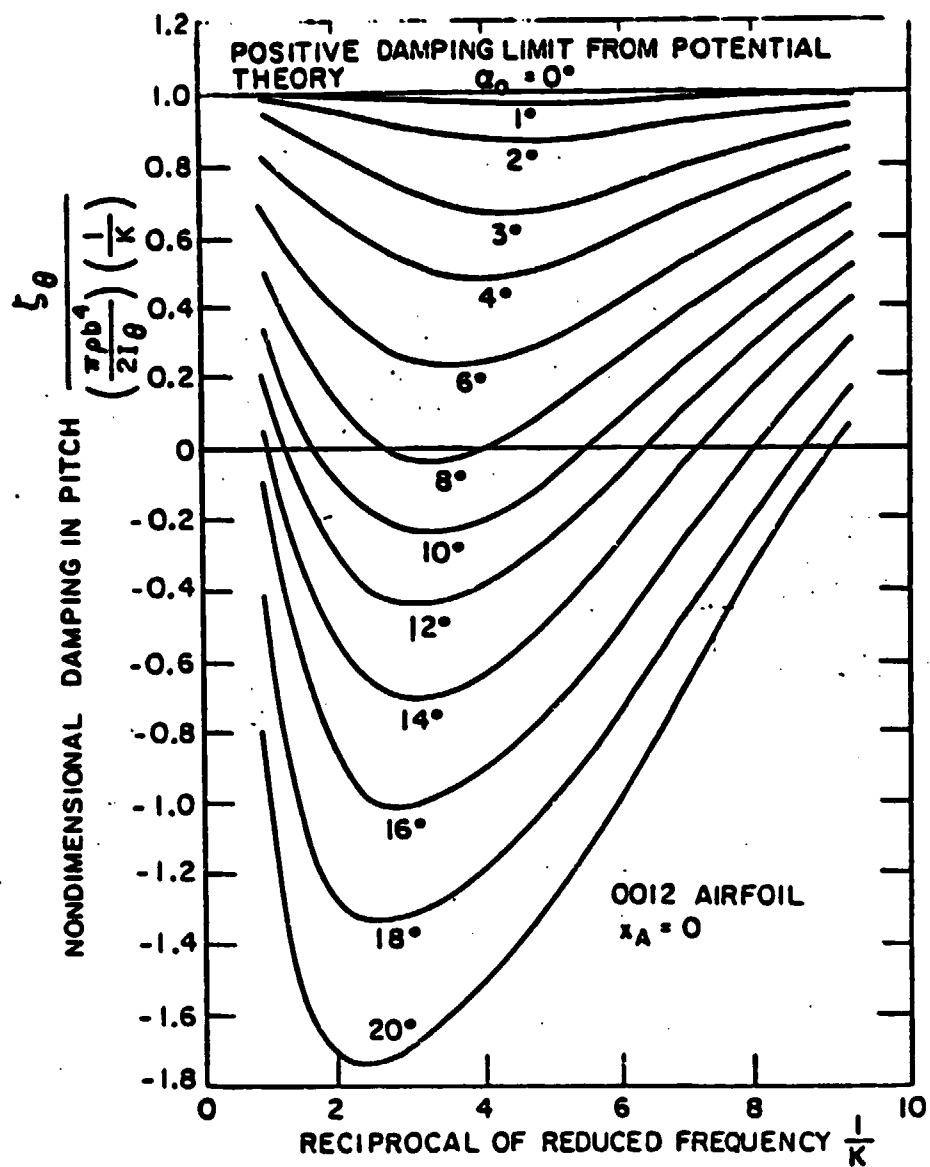


FIG. 3 Approximation for Generalized Pitch Damping

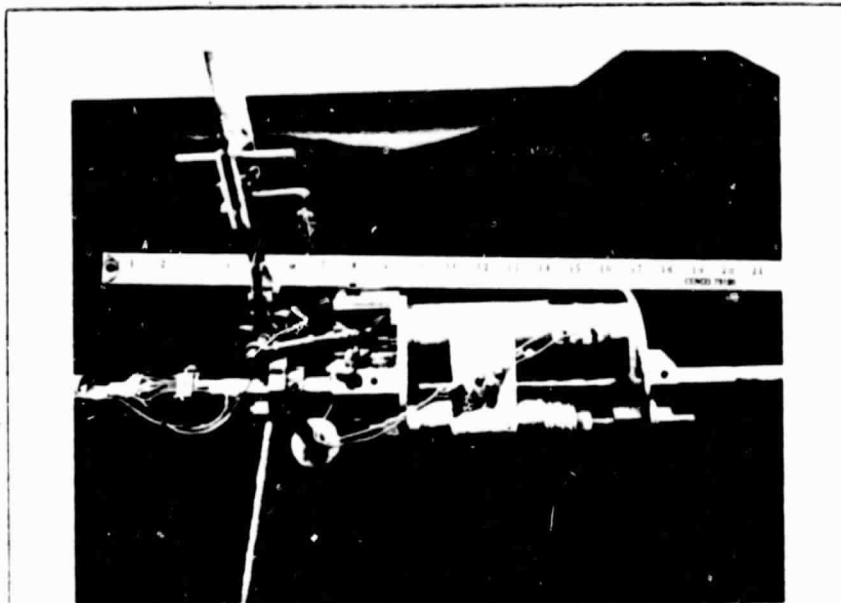


FIG. 4 Side View of Pitch Actuator and Blade Assembly

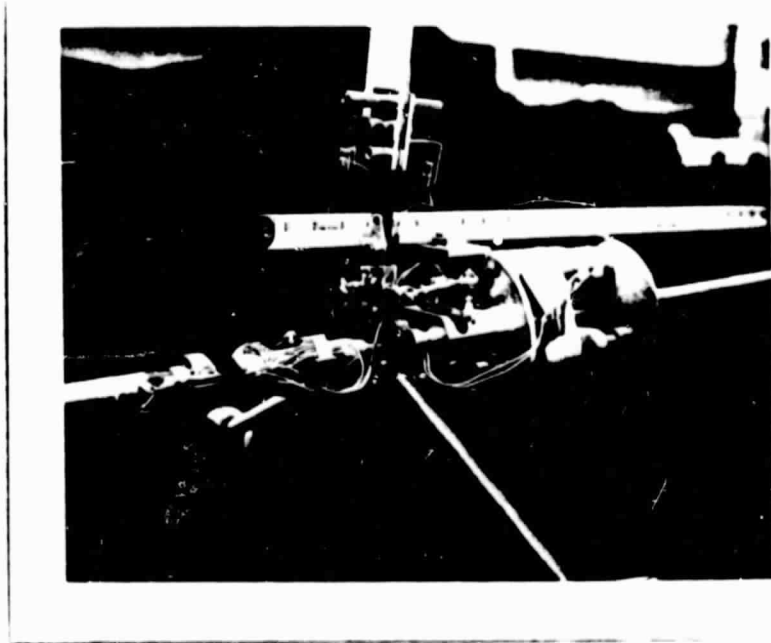


FIG. 5 3/4 View of Pitch Actuator and Blade Assembly

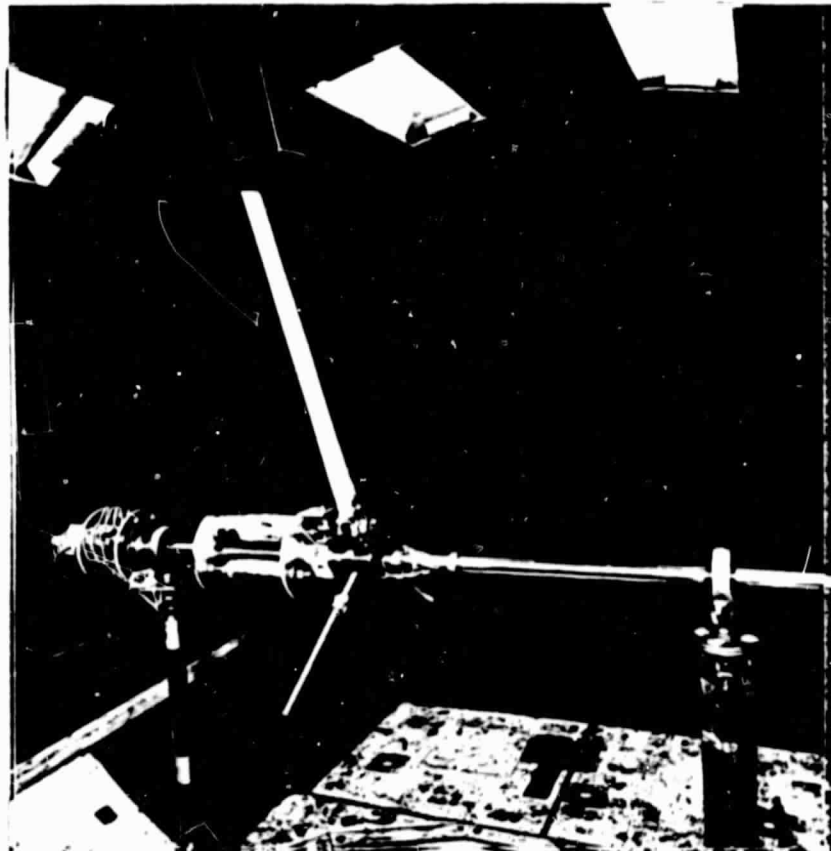
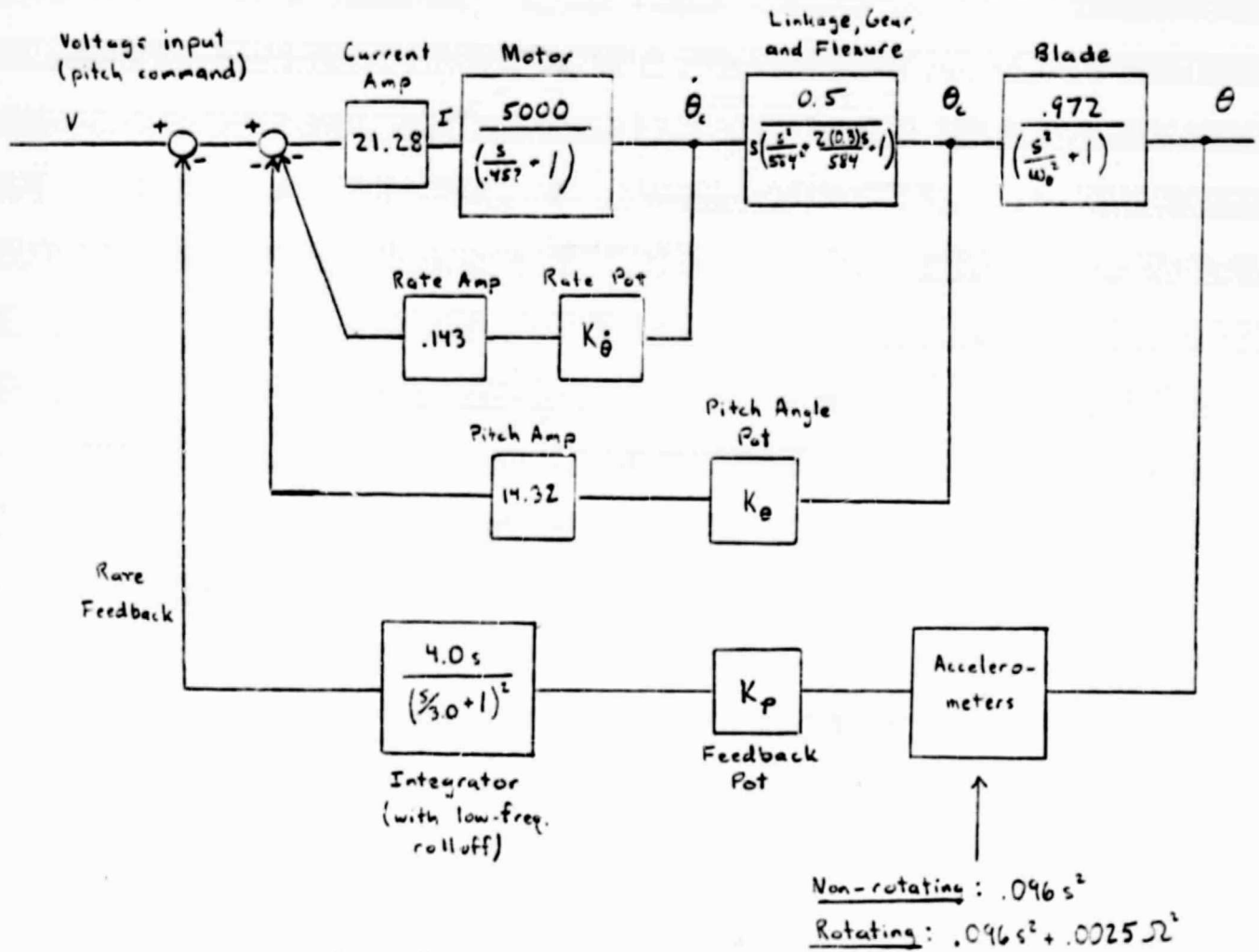


FIG. 6 Individual Blade Control Experimental Rig, Upstream View

ORIGINAL PAGE IS
OF POOR QUALITY



ω_0 = blade natural frequency
 (rad/sec)

$$K_F = (4.0)(K_p)(.096)(200)(.001)(1.0)(.102) = .00783 K_p$$

\uparrow integrator gain \uparrow accelerometer gain \uparrow volts per millivolt \uparrow g's per ms^{-2}

$$K_L = \text{total open loop gain} = (\text{forward loop gain})(K_F)$$

FIG. 7 Control System Block Diagram for "Electronic Spring" Tests

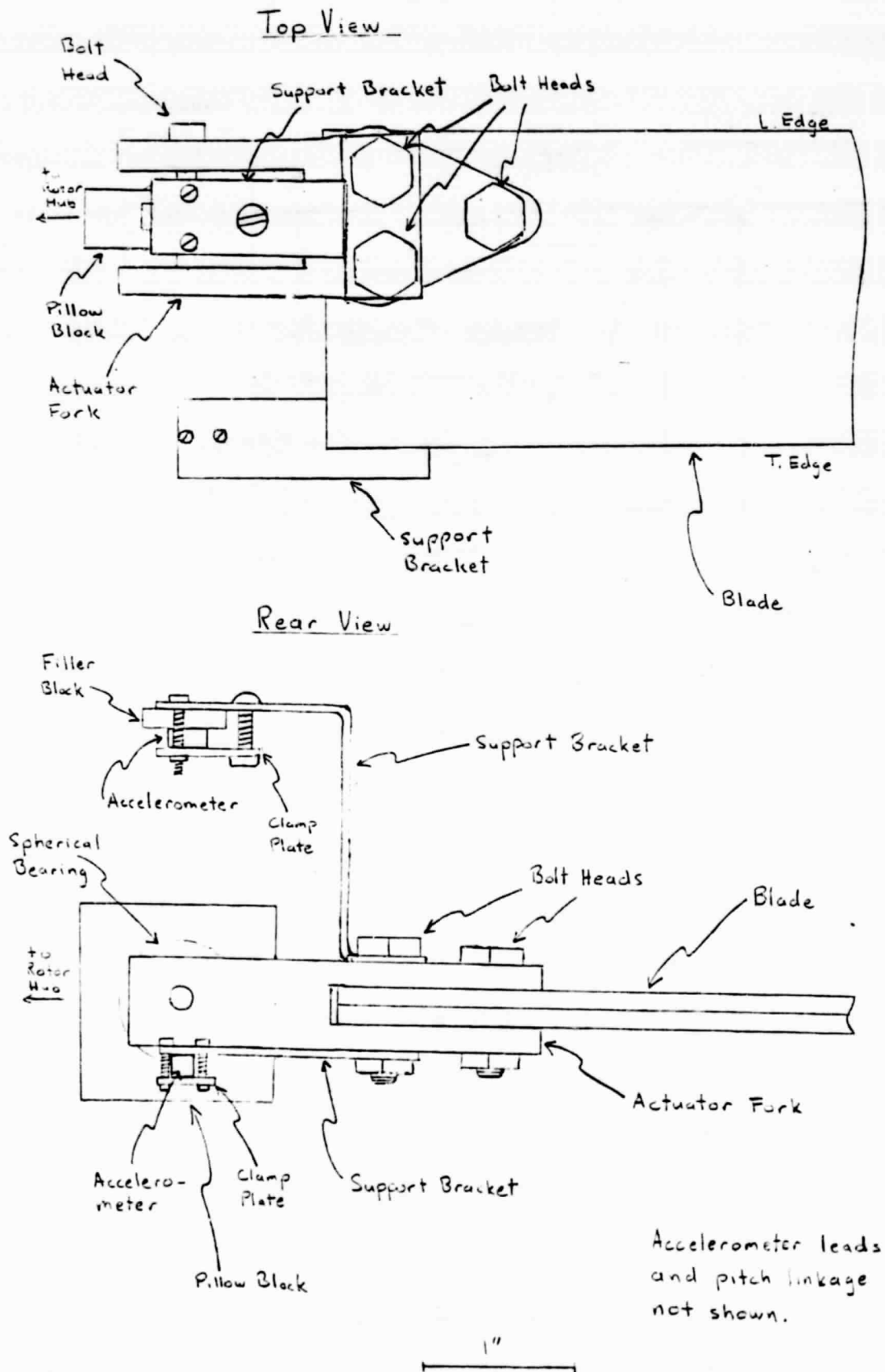
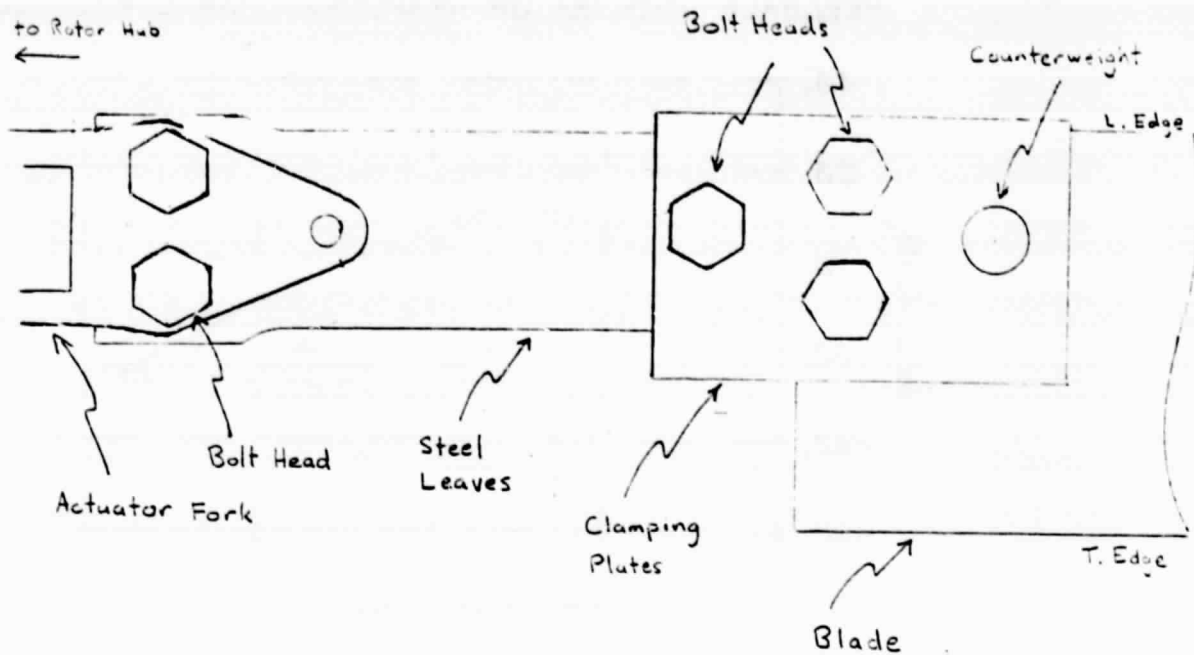


FIG. 8 Detail of Blade and Accelerometer Installation, "Electronic Spring" Configuration

Top View



Rear View

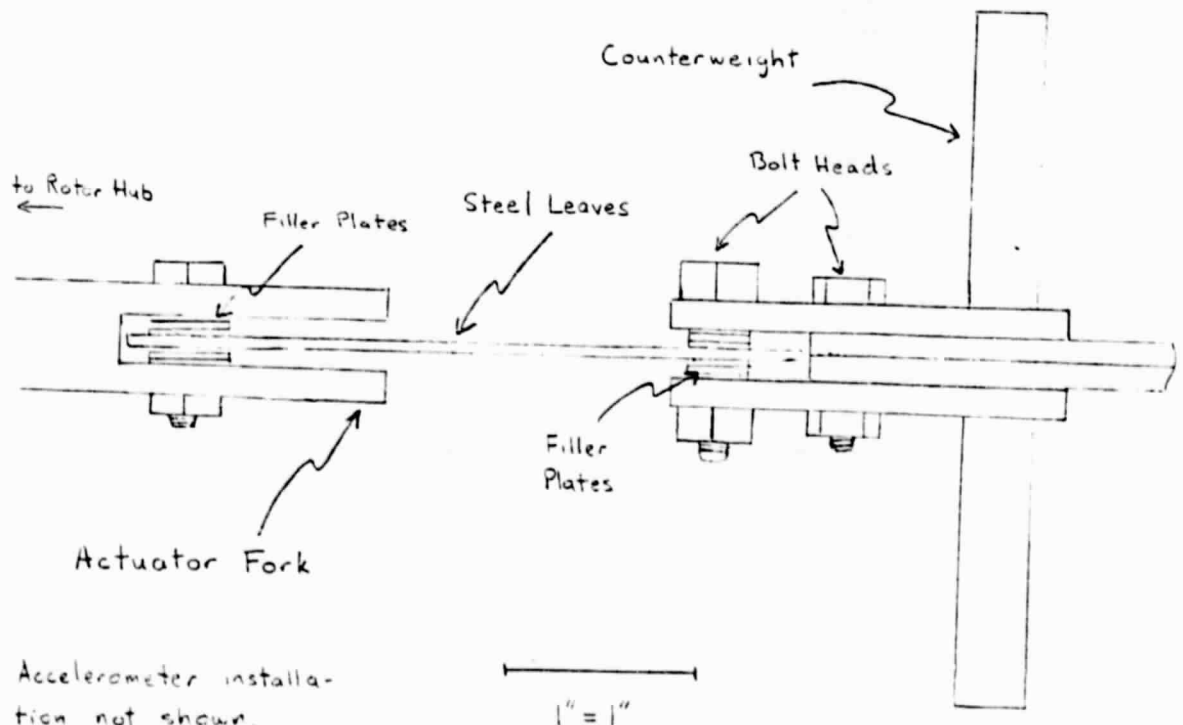


FIG. 9 Detail of Blade Installation, Mechanical Spring Configuration

FEEDBACK INTEGRATOR RESPONSE CHARACTERISTIC

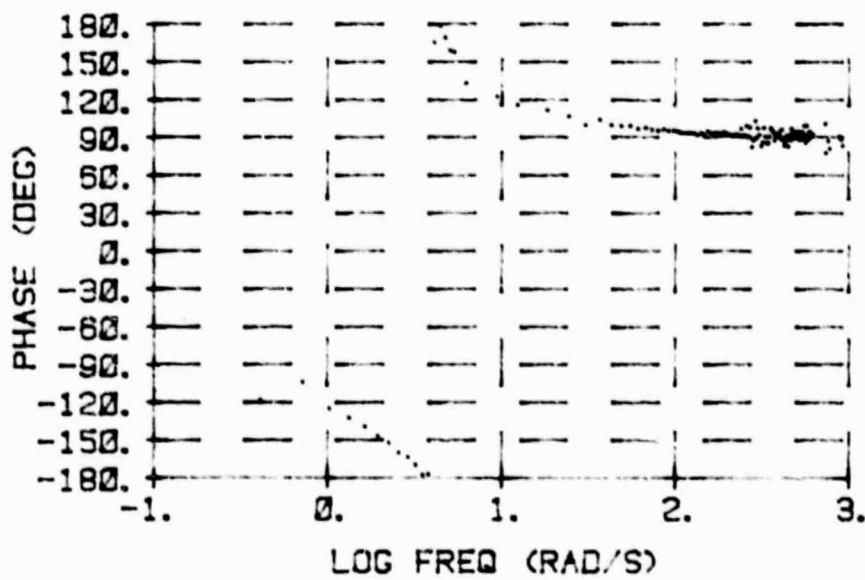
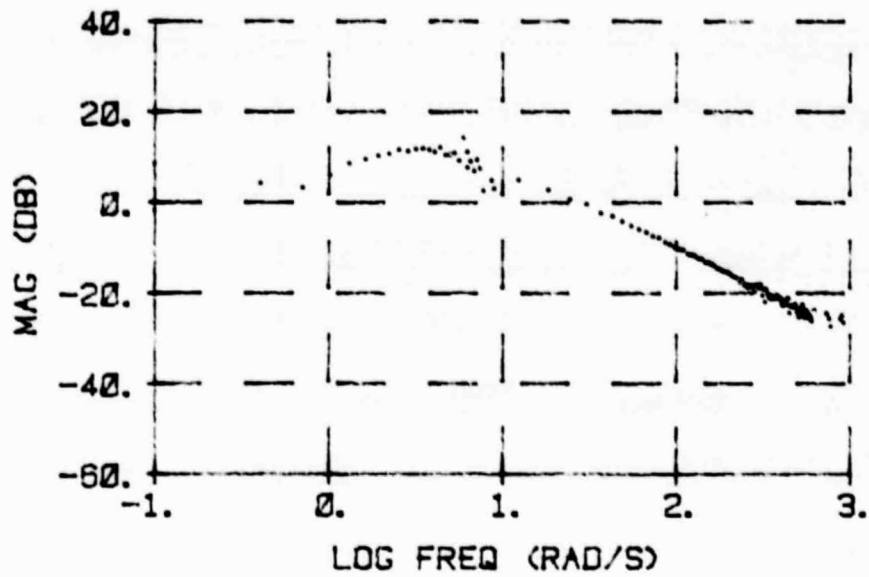


FIG. 10 Integrator Frequency Response

$$K_{\theta} = .234$$

$$K_{\dot{\theta}} = .05$$

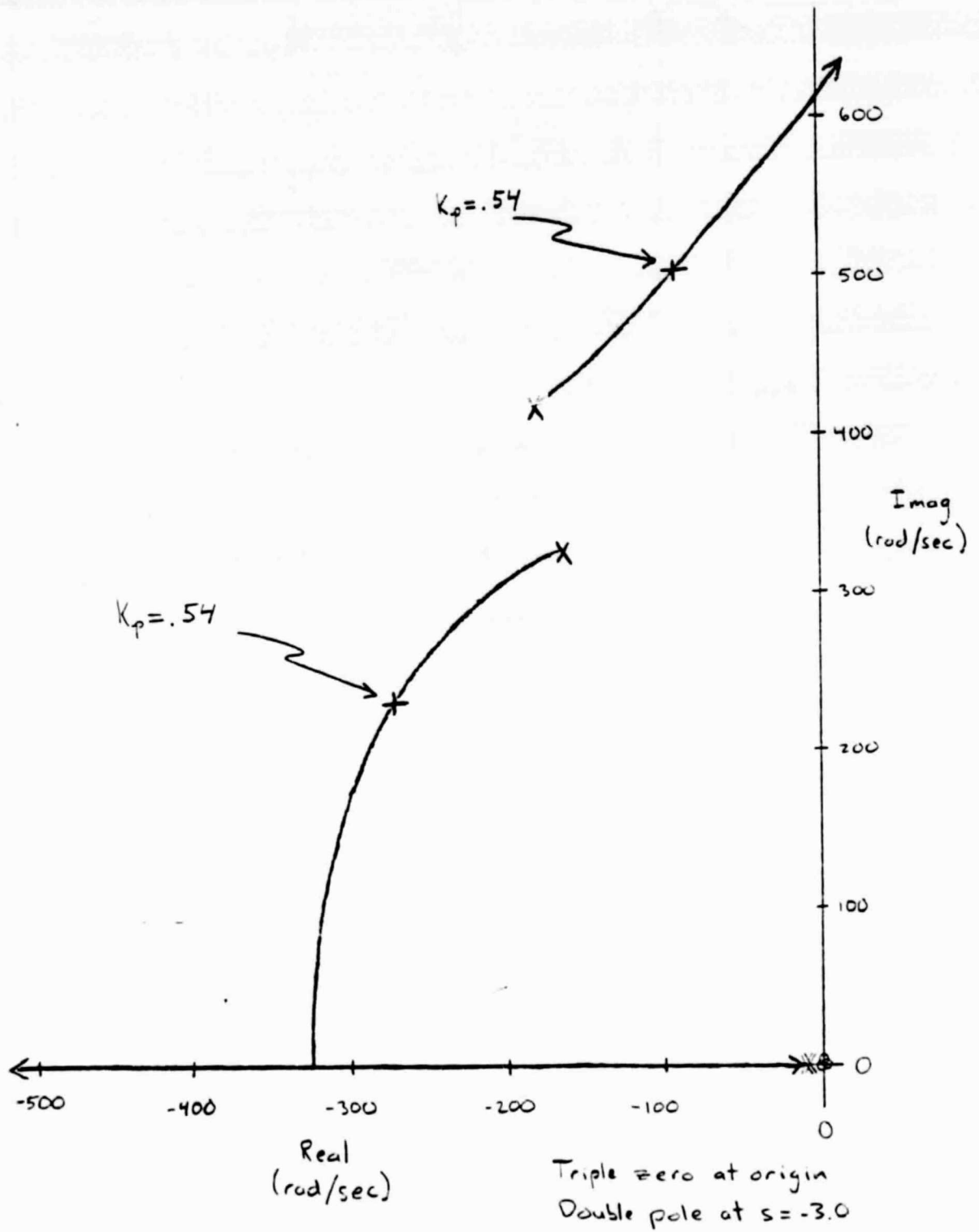
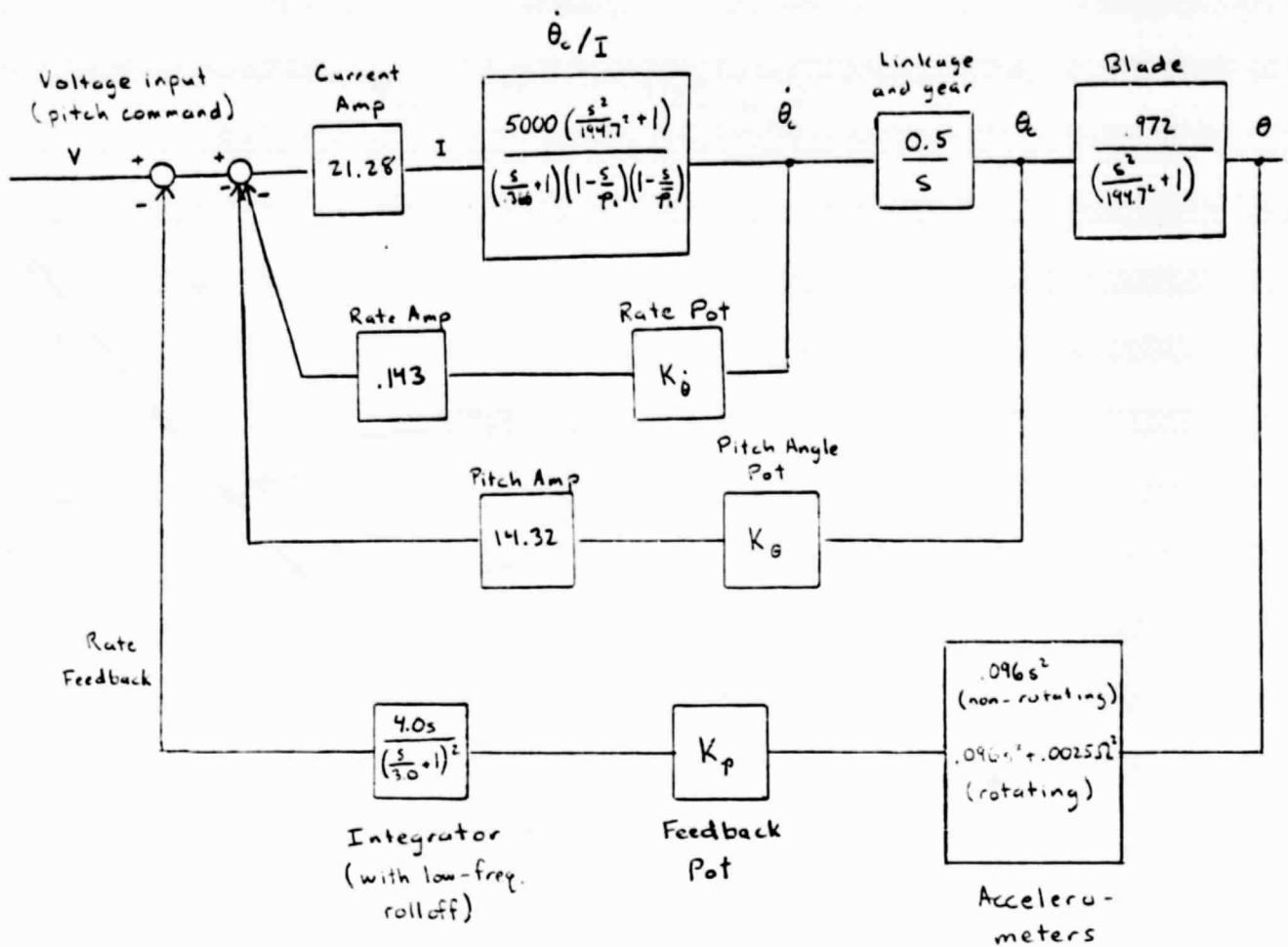


FIG. 11 Root Locus Diagram, "Electronic Spring" Static Test



$$K_{\theta} = .528$$

$$K_{\dot{\theta}} = .19$$

$$K_p = 0.0, 0.13, 0.26$$

$$p_1 = -.057 + 220.1j \text{ for } \omega = 0$$

Definitions of the feedback gain K_F and the total

open loop gain K_L are the same as in Fig. 7.

(See Appendix 2 for details of system dynamics.)

FIG. 12 Control System Block Diagram for Mechanical Spring Tests

$$K_{\theta} = 0.528$$

$$K_{\dot{\theta}} = 0.14$$

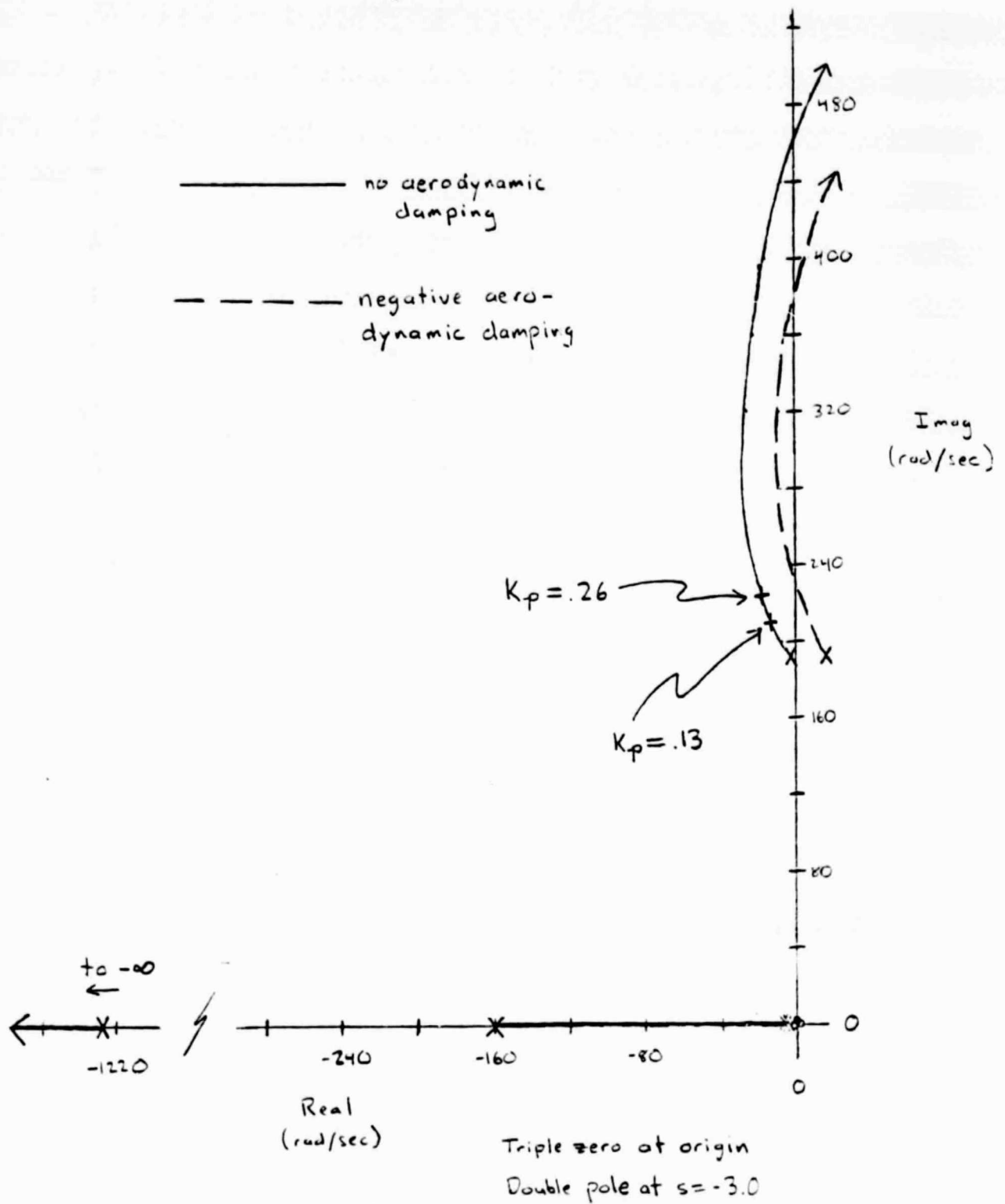


FIG. 13 Root Locus Diagrams, Static Tests with Mechanical Spring

$$K_{\theta} = .528$$

$$K_{\dot{\theta}} = .08$$

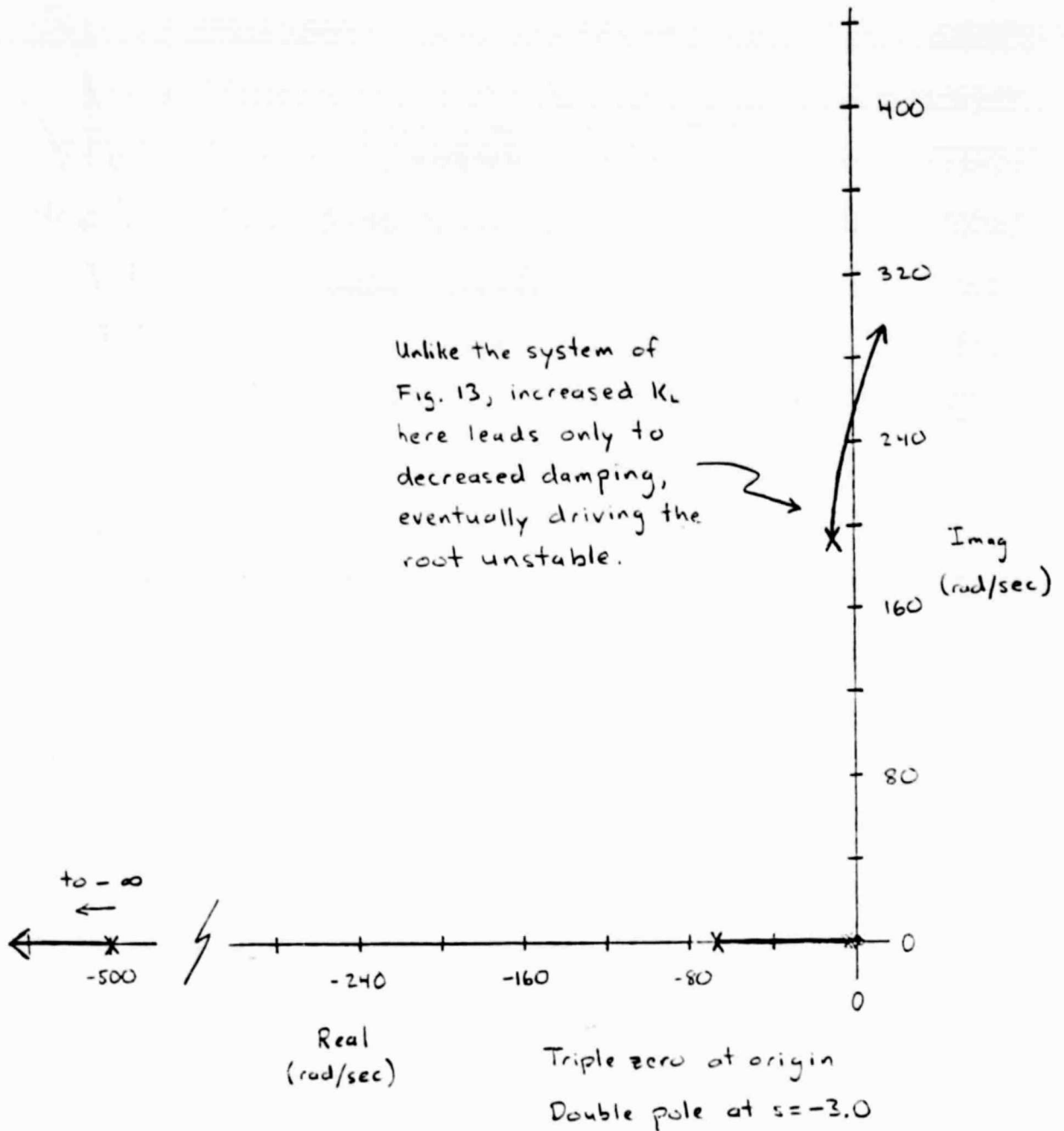
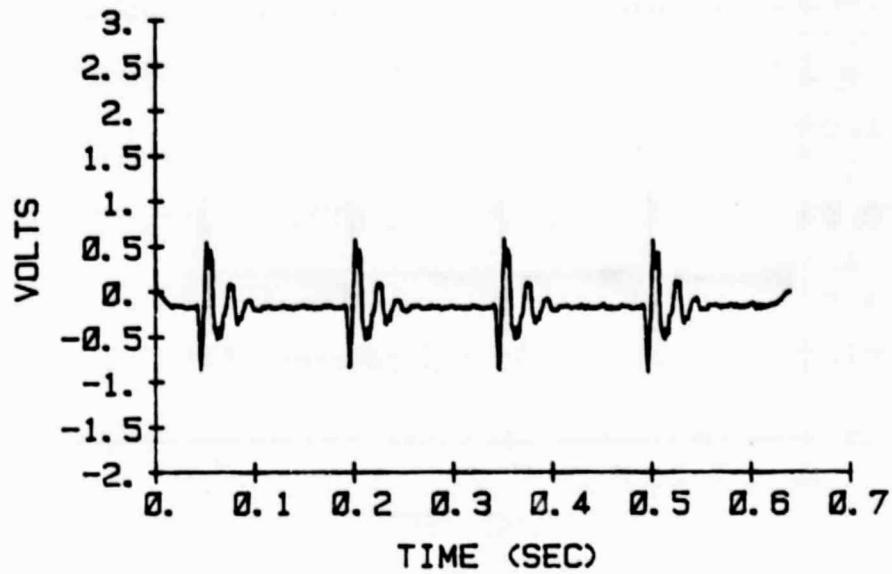


FIG. 14 Root Locus Diagram, Static System with Low K_{θ}

PITCH RATE, $KP=0.0$



PITCH ACCELERATION, $KP=0.0$

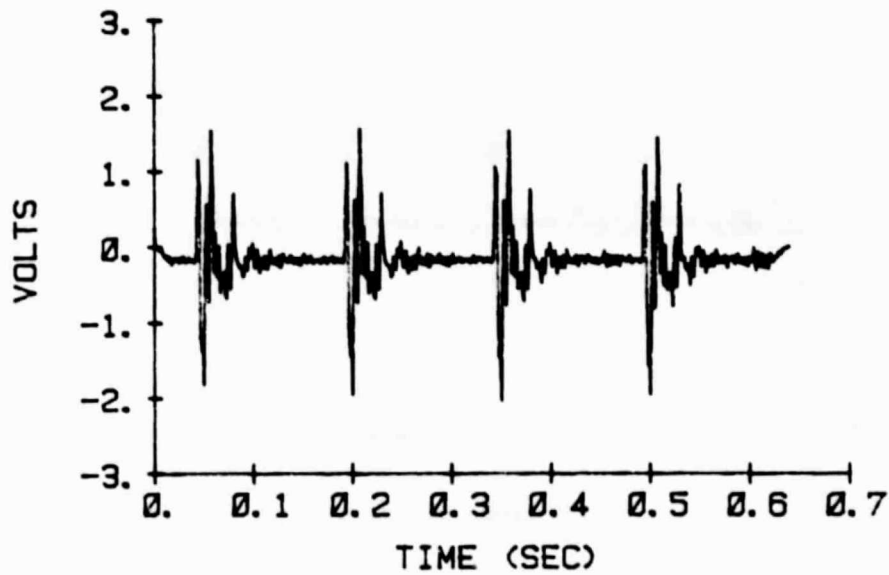
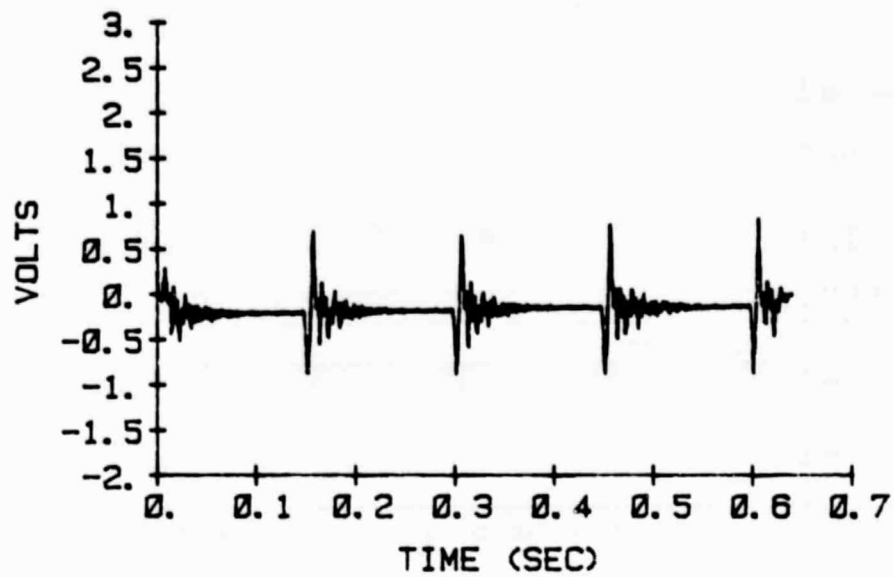


FIG. 15 Open-Loop, Static "Electronic Spring" Tests

PITCH RATE, $KP=0.54$



PITCH ACCELERATION, $KP=0.54$

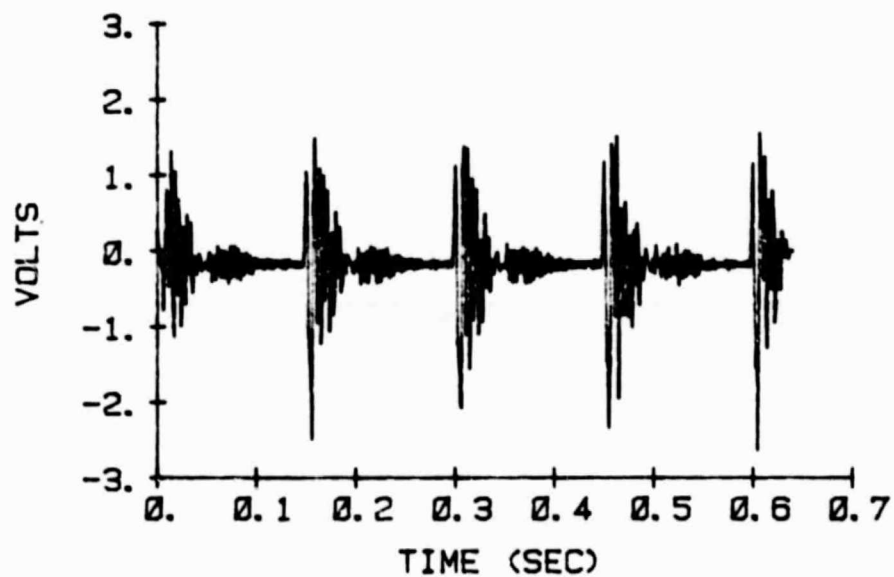
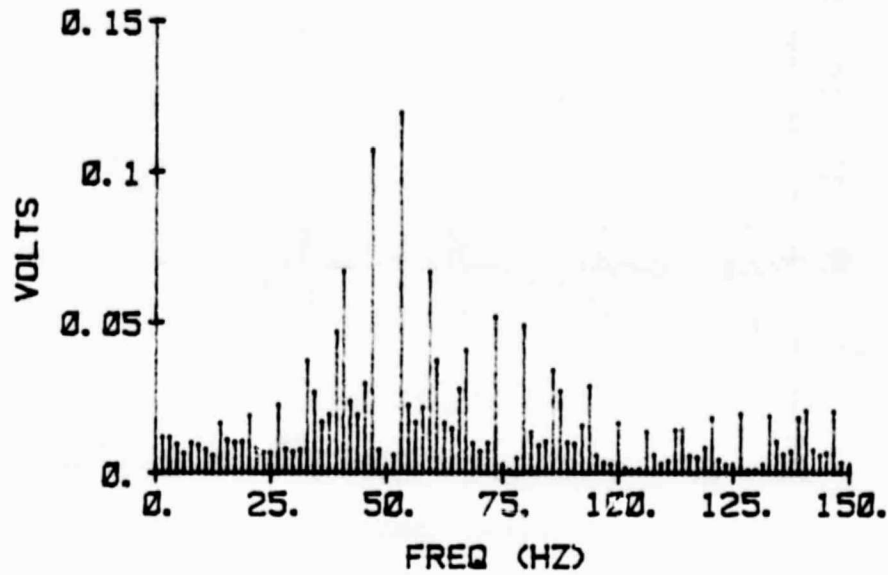


FIG. 16 Closed-Loop, Static "Electronic Spring" Tests

FFT OF PITCH RATE, $KP=0.0$



FFT OF PITCH RATE, $KP=0.54$

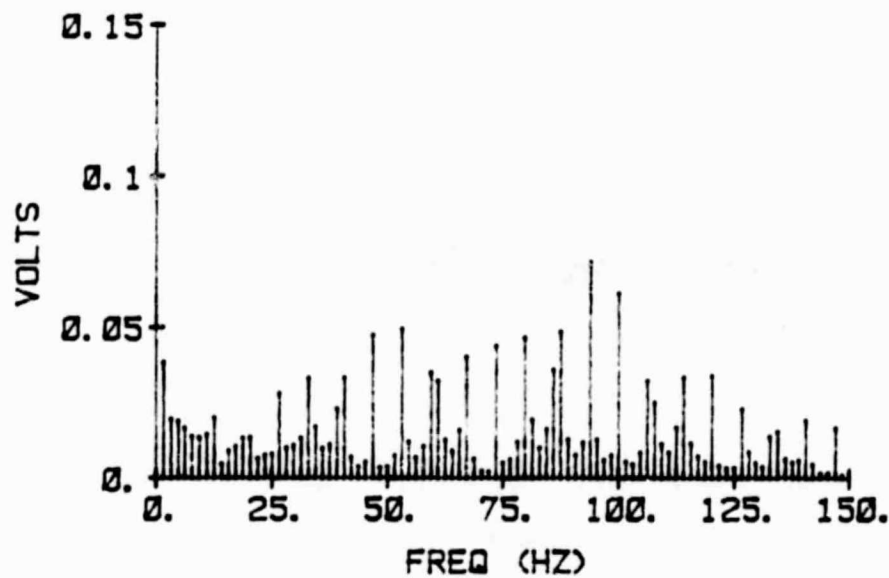


FIG. 17 Fourier Transforms of Static "Electronic Spring" Responses

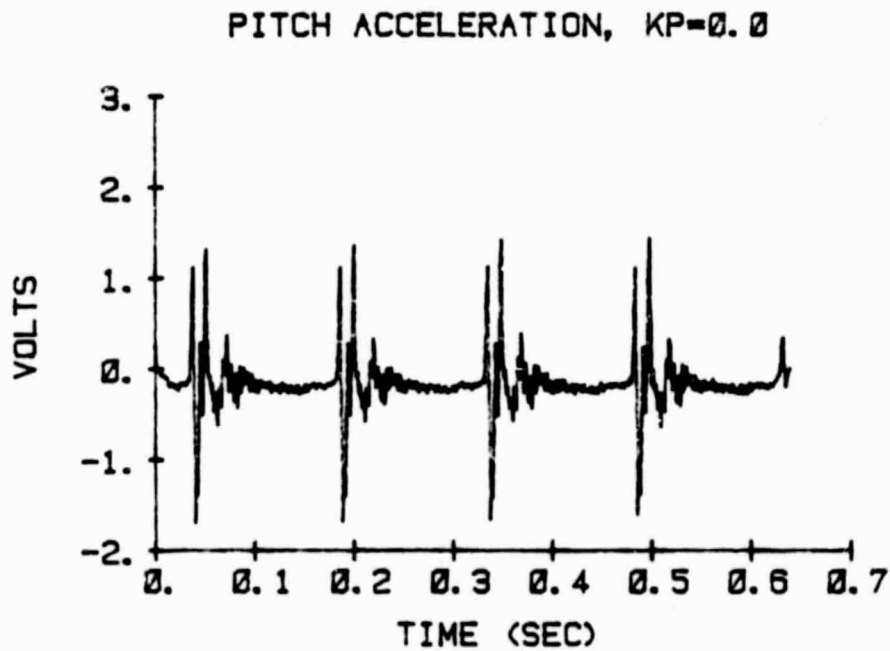
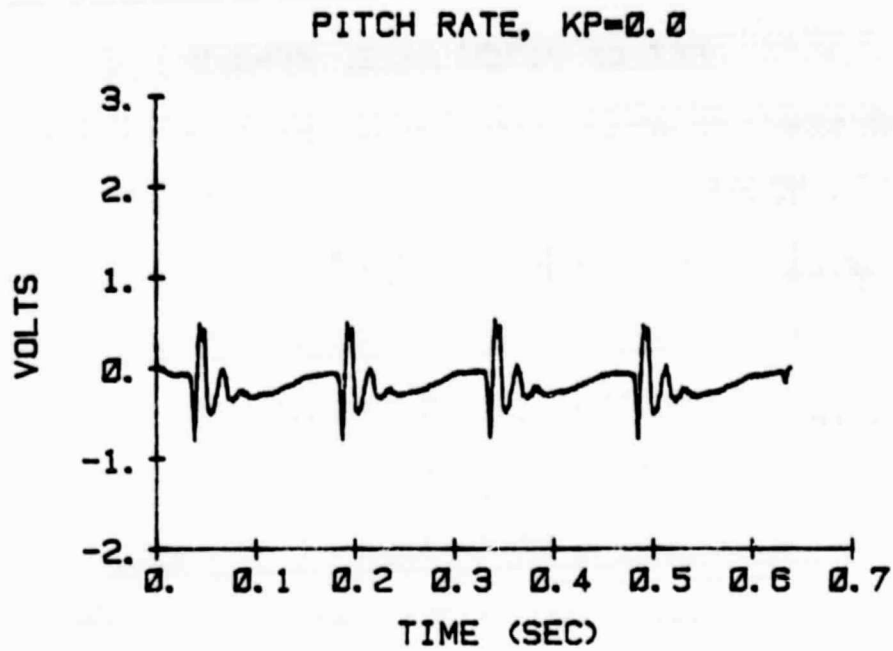


FIG. 18 Open-Loop "Electronic Spring" Tests, $\Omega = 6.2$ Hz

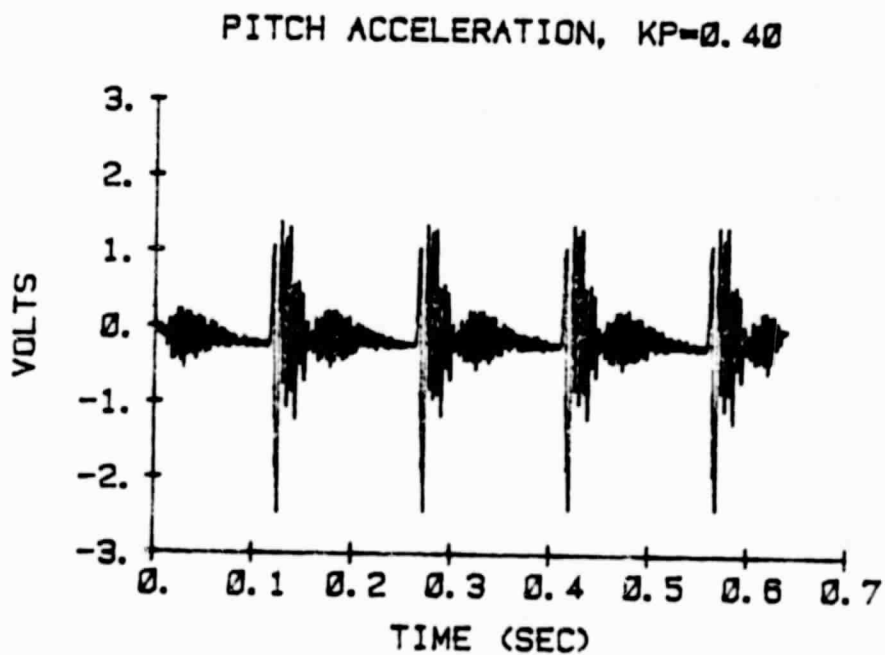
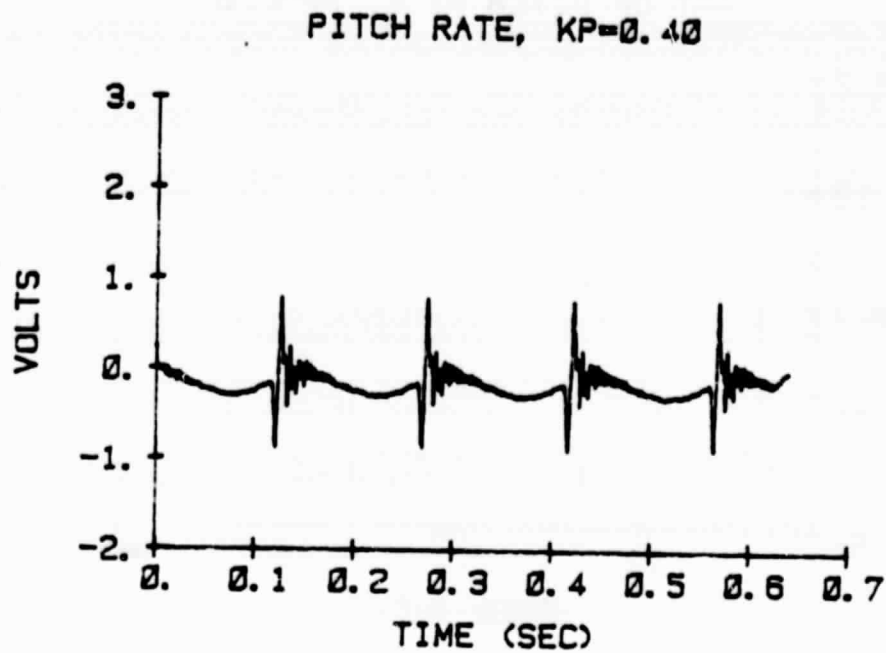
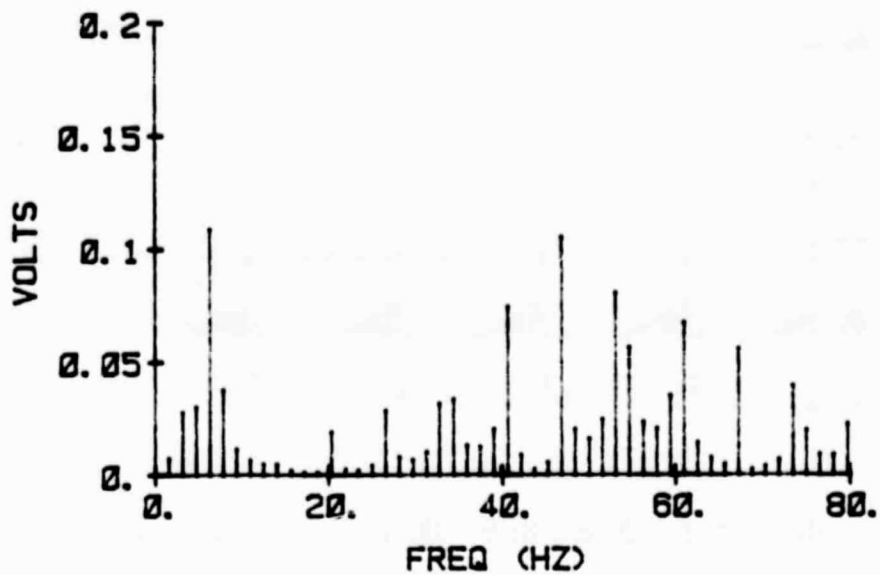


FIG. 19 Closed-Loop "Electronic Spring" Tests, $\Omega = 6.2$ Hz

FFT OF PITCH RATE, $KP=0.0$



FFT OF PITCH RATE, $KP=0.40$

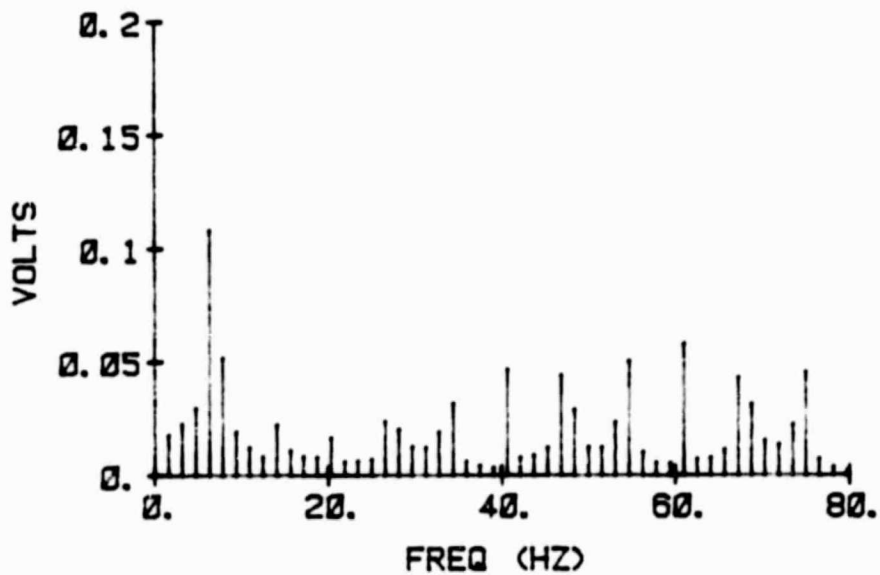
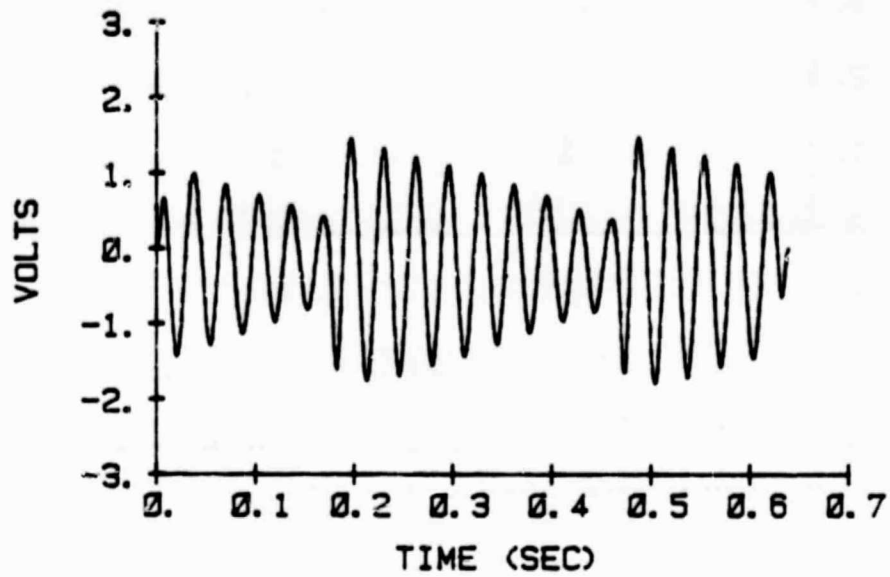


FIG. 20 Fourier Transforms of "Electronic Spring" Responses,
 $\Omega = 6.2$ Hz

PITCH RATE, $KP=0.0$



PITCH ACCELERATION, $KP=0.0$

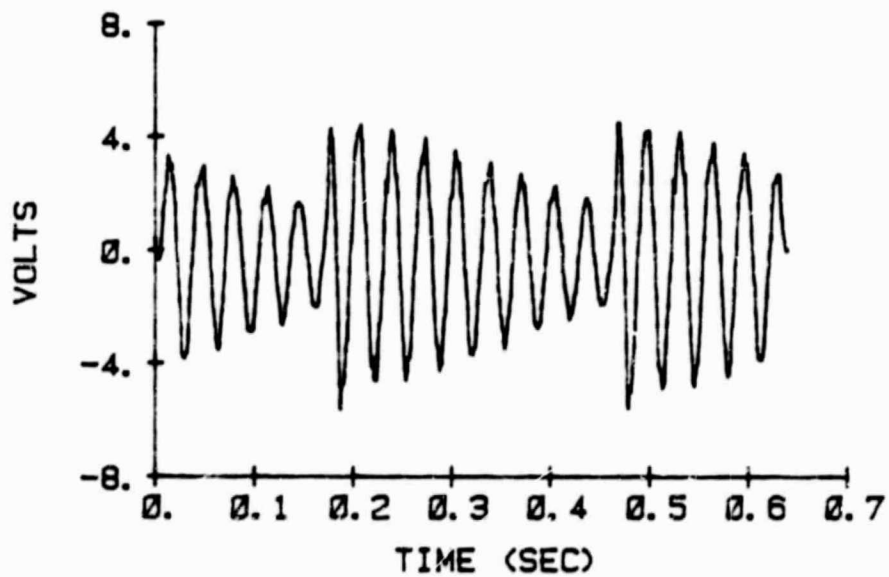


FIG. 21 Open-Loop, Static Mechanical Spring Tests

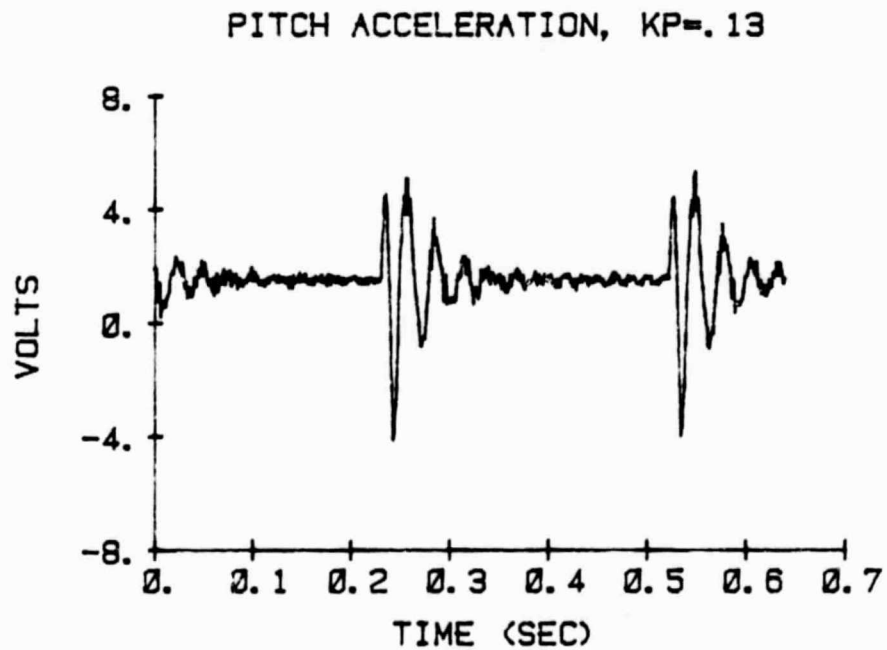
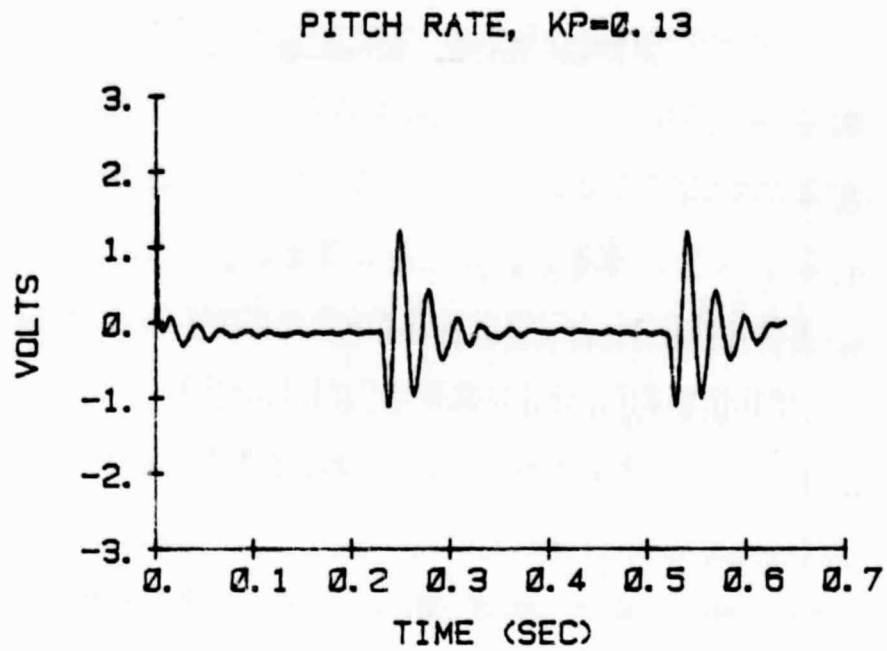
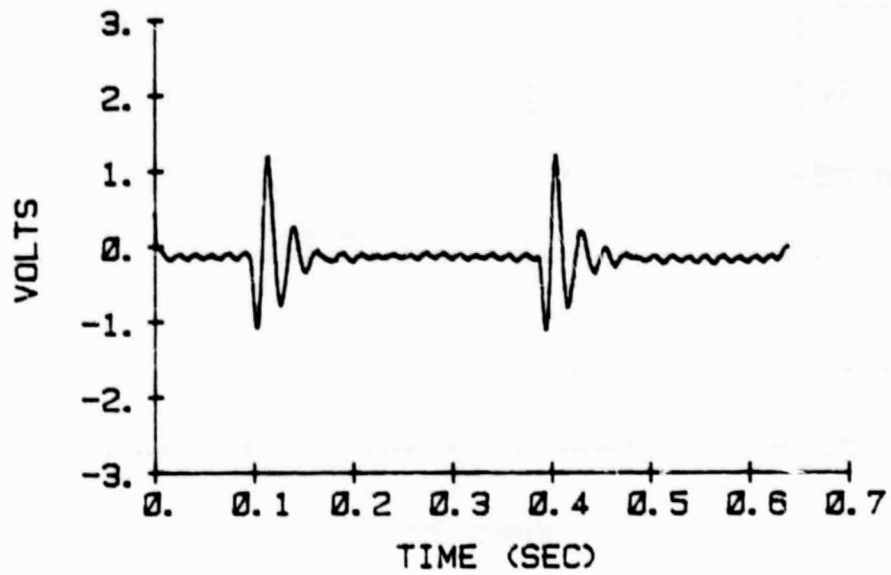


FIG. 22 Static Mechanical Spring Tests, Moderate Feedback

PITCH RATE, $KP=.26$



PITCH ACCELERATION, $KP=.26$

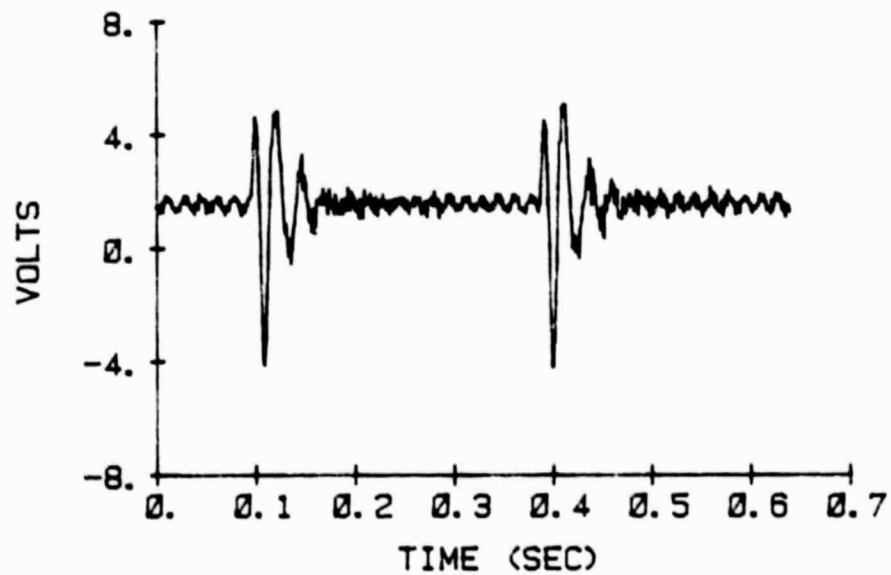
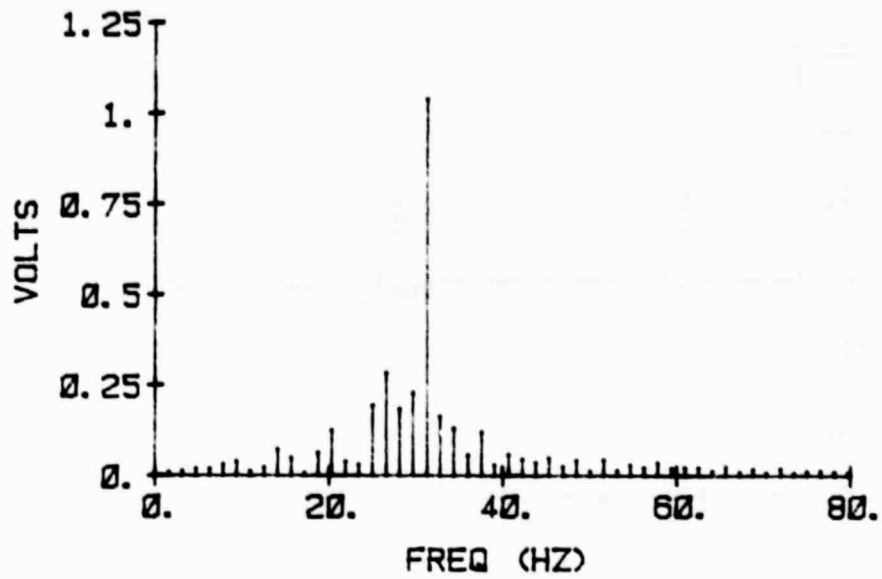


FIG. 23 Static Mechanical Spring Tests, High Feedback

FFT OF PITCH RATE, $KP=0.0$



FFT OF PITCH RATE, $KP=0.26$

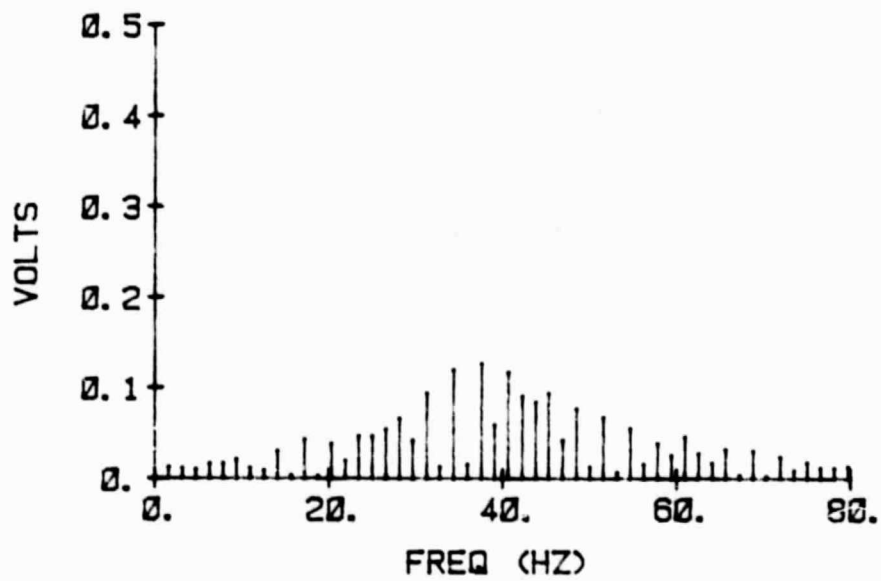


FIG. 24 Fourier Transforms of Static Mechanical Spring Responses

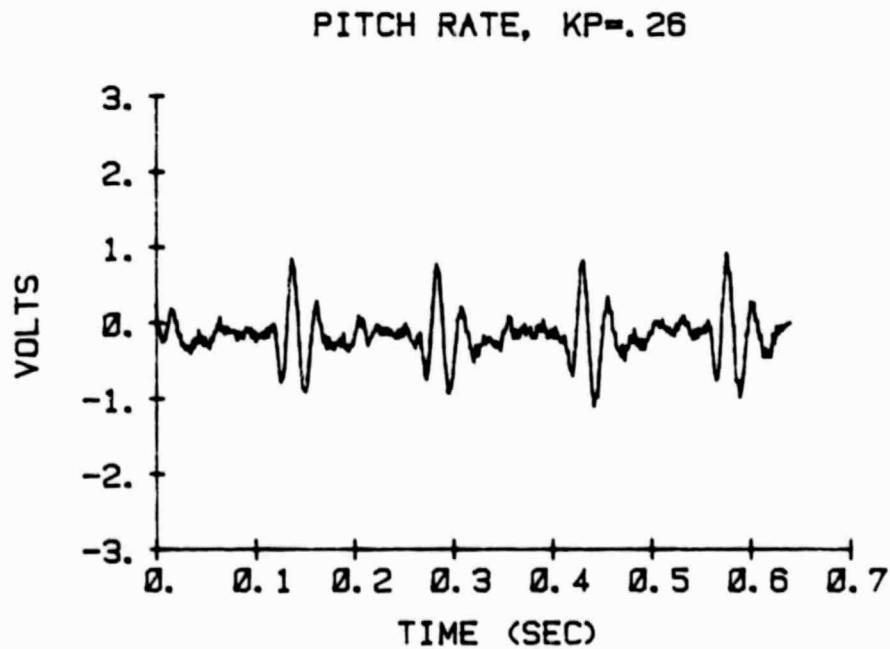
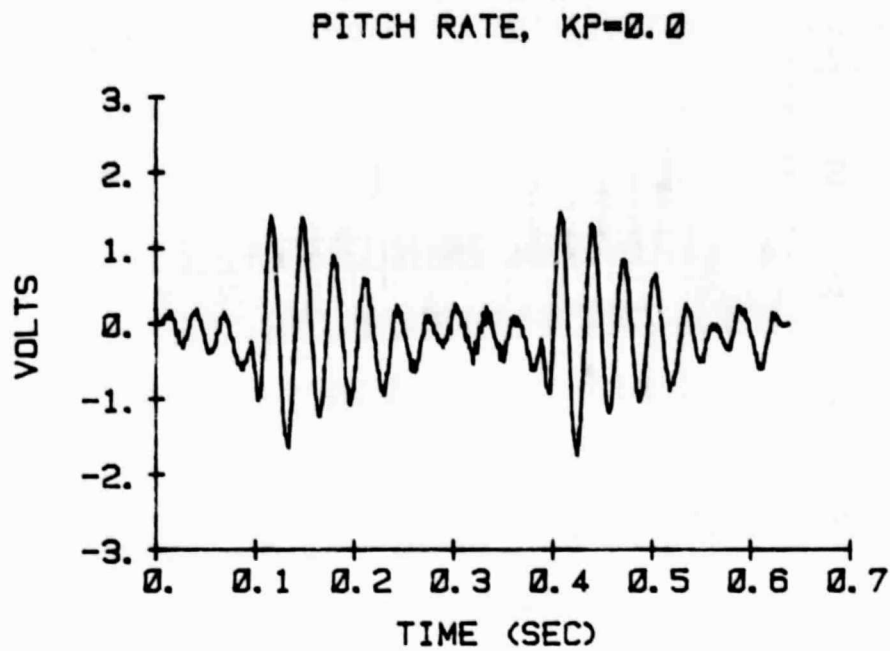


FIG. 25 Open-Loop and High Feedback Mechanical Spring Tests,
 $\Omega = 6.7 \text{ Hz}$, $\mu = 0.0$

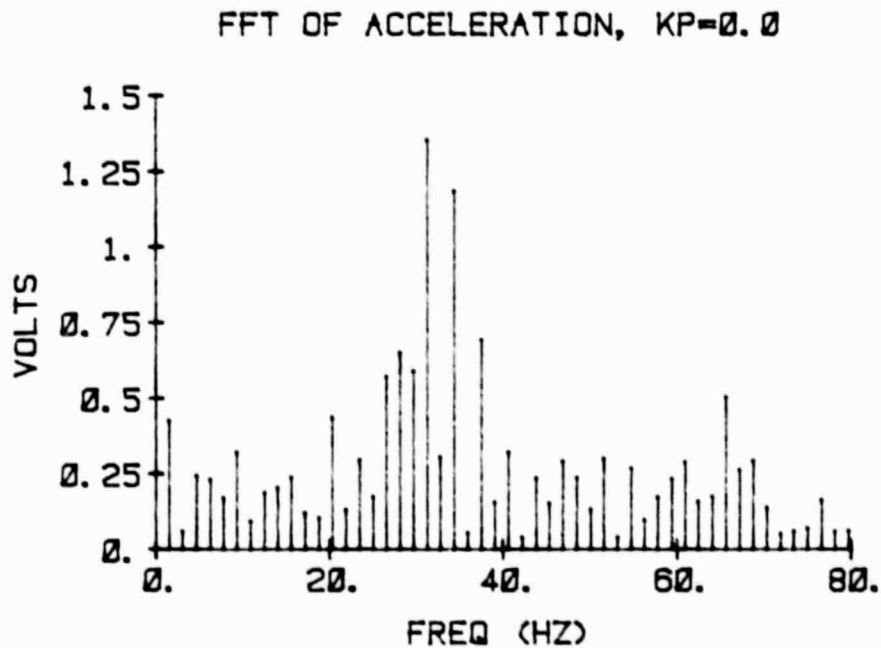
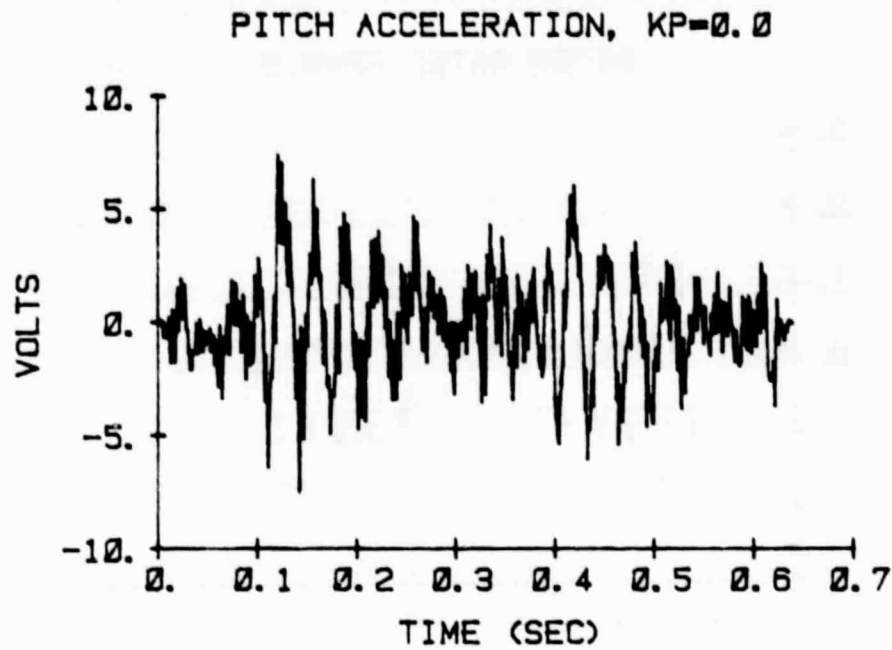


FIG. 26 Open-Loop, Mechanical Spring Test, $\Omega = 6.7$ Hz, $\mu = 0.0$

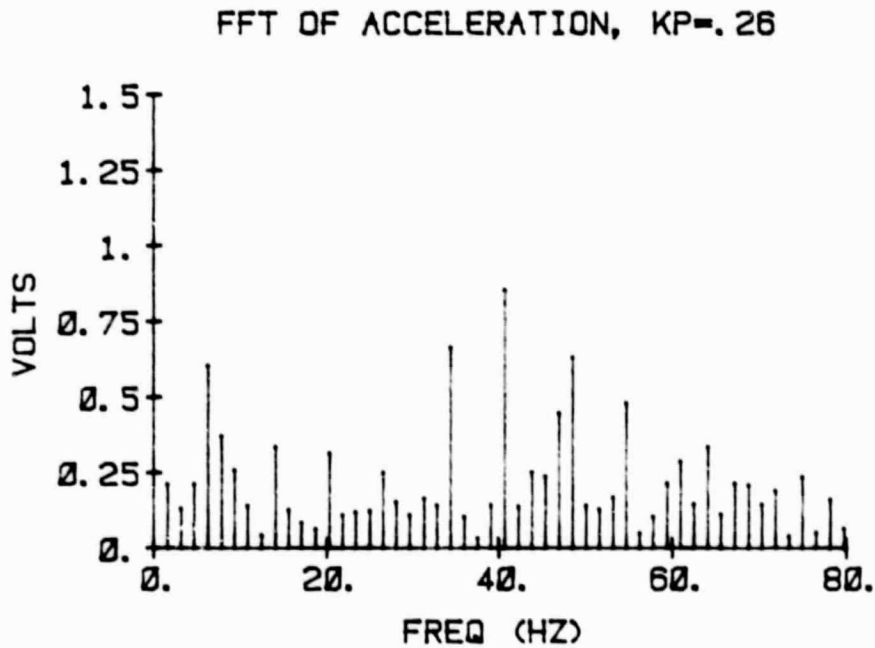
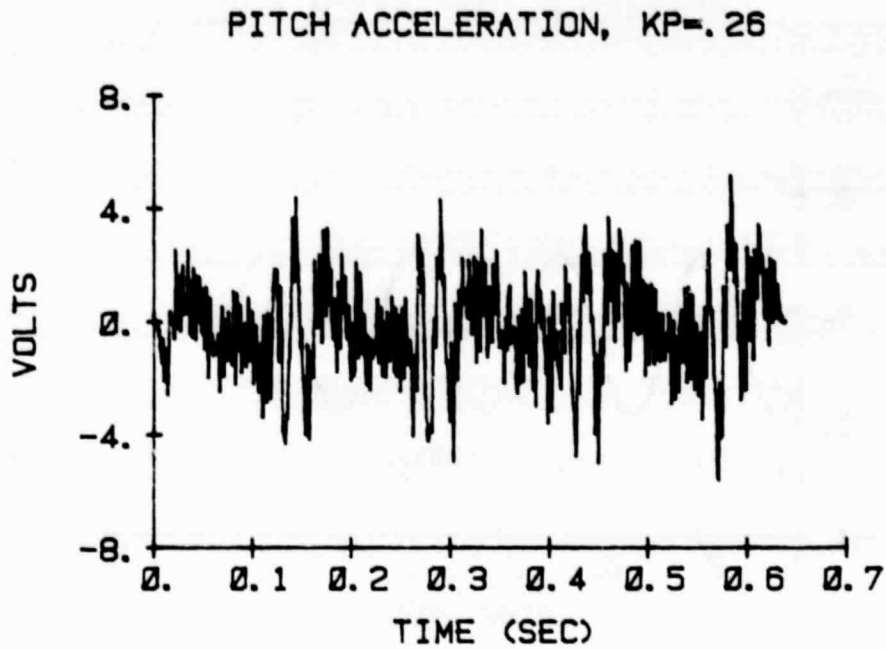
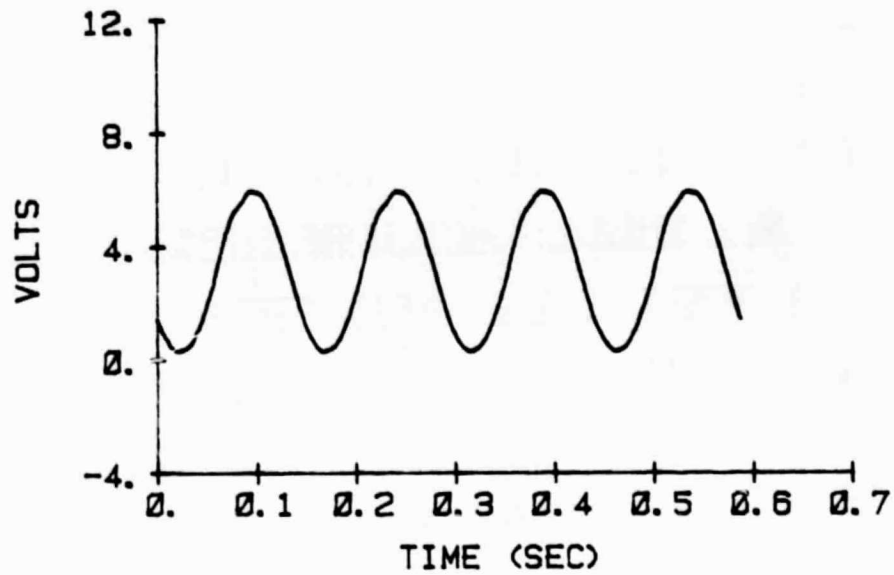


FIG. 27 High Feedback Mechanical Spring Test, $\Omega = 6.7$ Hz,
 $\mu = 0.0$

FORWARD FLIGHT PITCH INPUT



0 v. = 6° pitch
at root
3.2° per volt

PITCH RATE, $K_P=0.0$

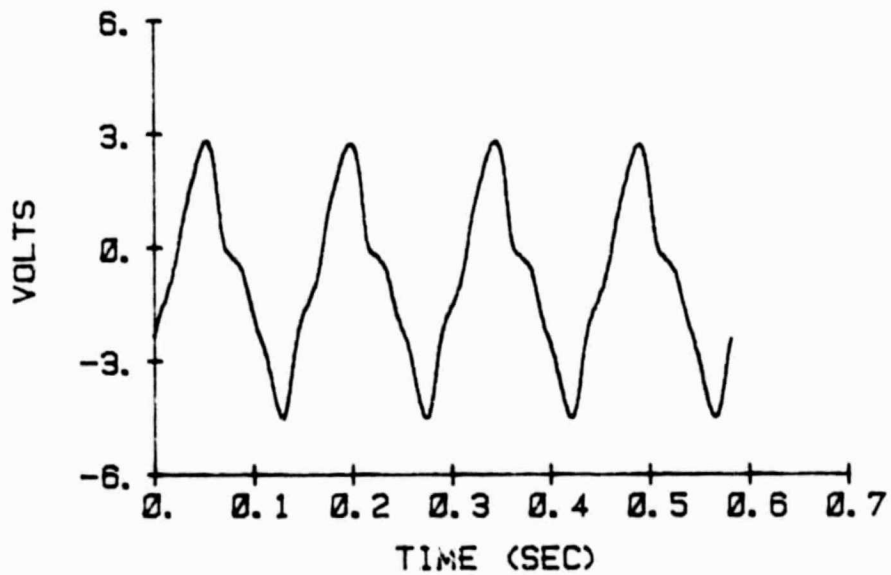


FIG. 28 Open-Loop, Mechanical Spring Test, $\Omega = 6.7$ Hz, $\mu = 0.30$

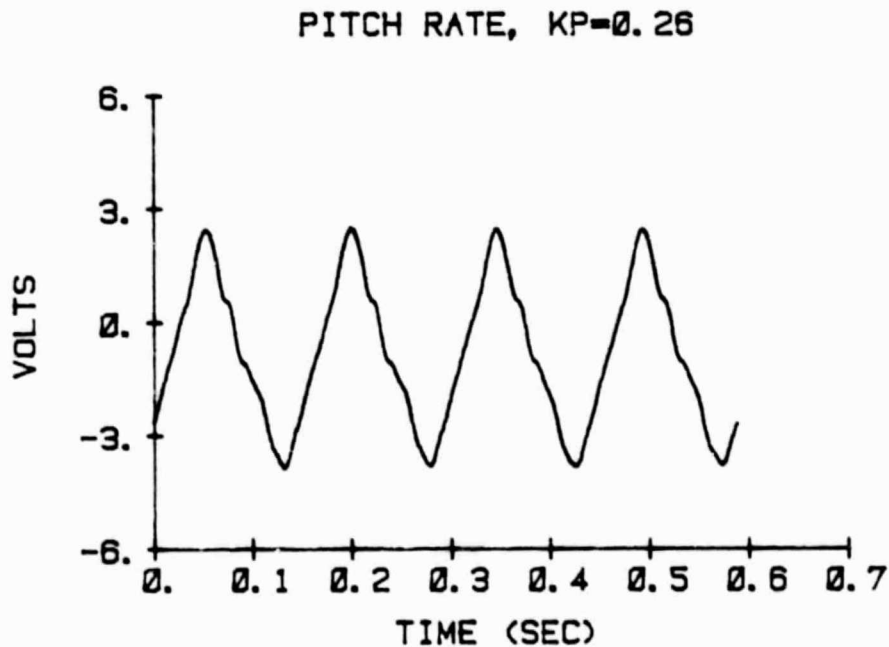
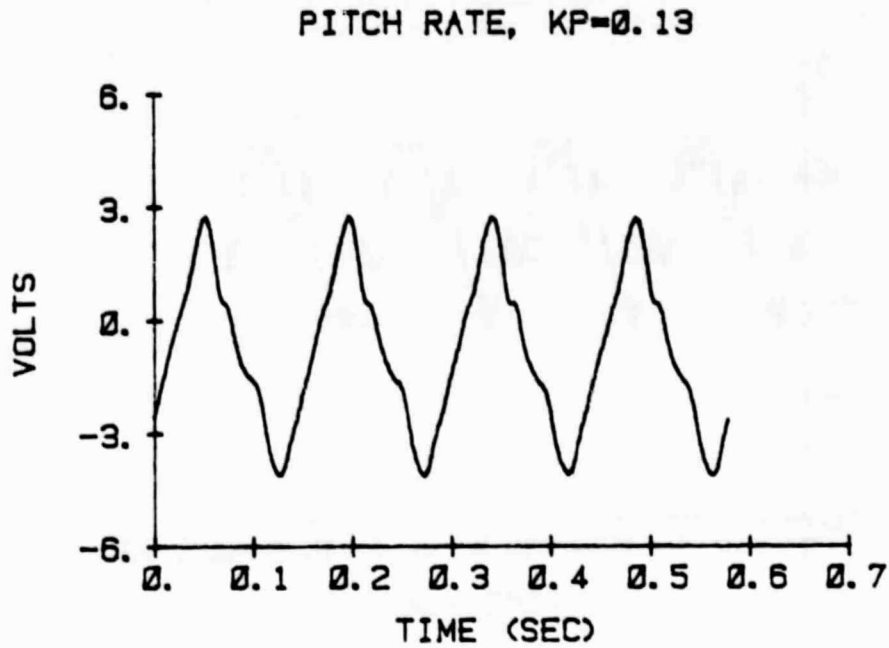


FIG. 29 Moderate and High Feedback Mechanical Spring Tests,
 $\Omega = 6.7 \text{ Hz}$, $\mu = 0.30$

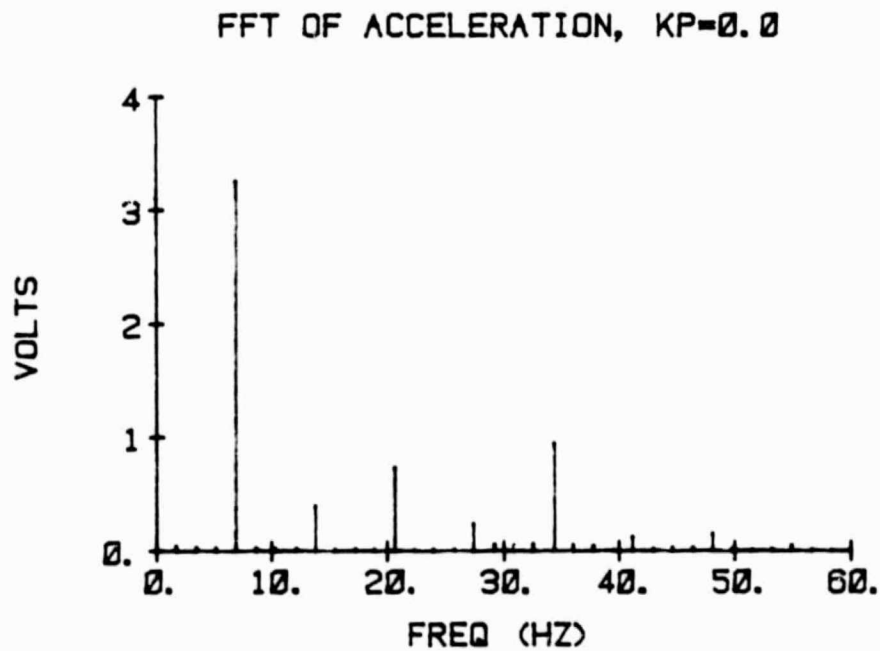
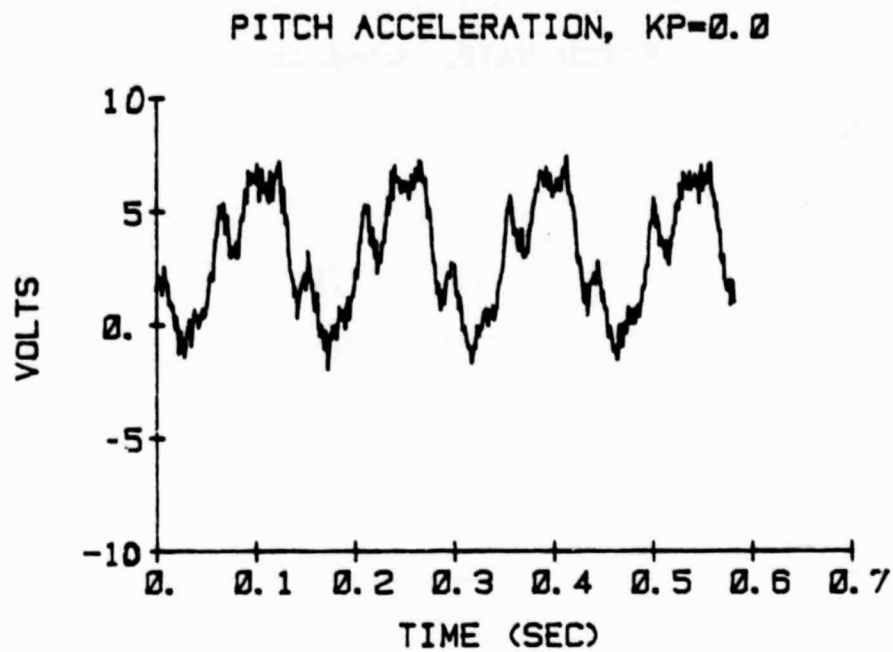
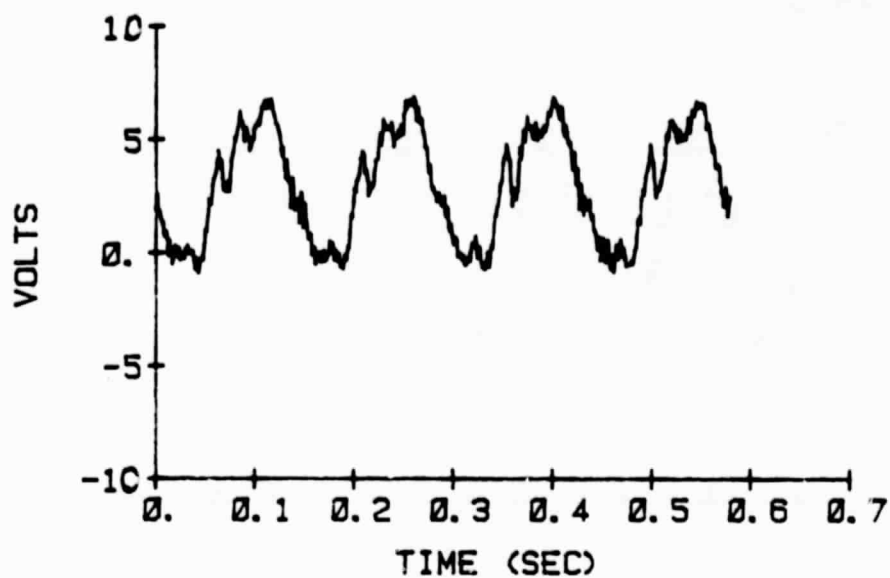


FIG. 30 Open-Loop, Mechanical Spring Test, $\Omega = 6.7$ Hz,
 $\mu = 0.30$

PITCH ACCELERATION, $KP=.13$



FFT OF ACCELERATION, $KP=.13$

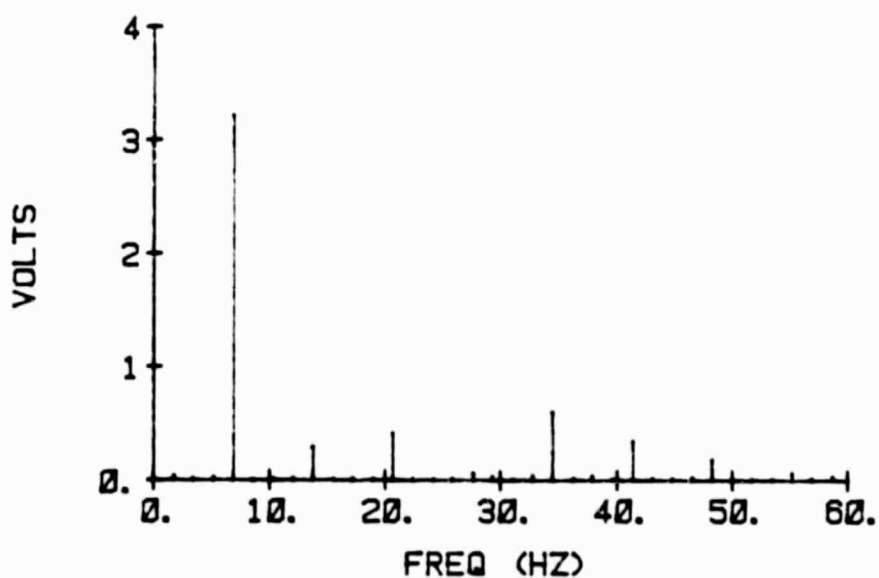
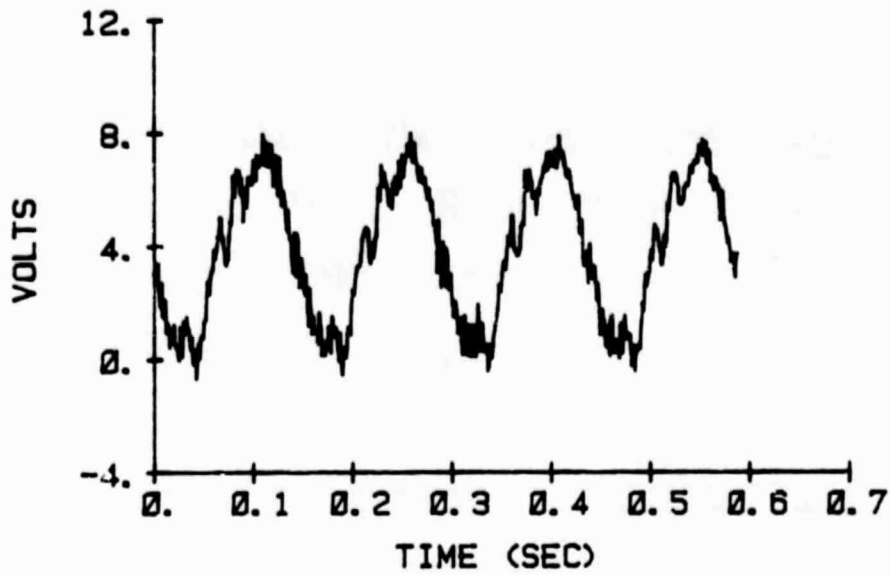


FIG. 31 Moderate Feedback, Mechanical Spring Test, $\Omega = 6.7$ Hz,
 $\mu = 0.30$

PITCH ACCELERATION, $KP=.26$



FFT OF ACCELERATION, $KP=.26$

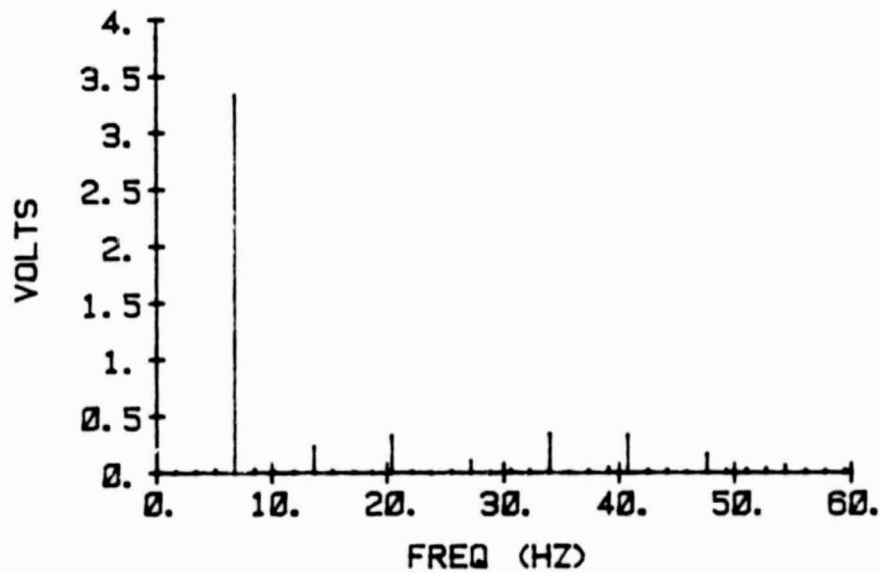


FIG. 32 High Feedback, Mechanical Spring Test, $\Omega = 6.7$ Hz,
 $\mu = 0.30$

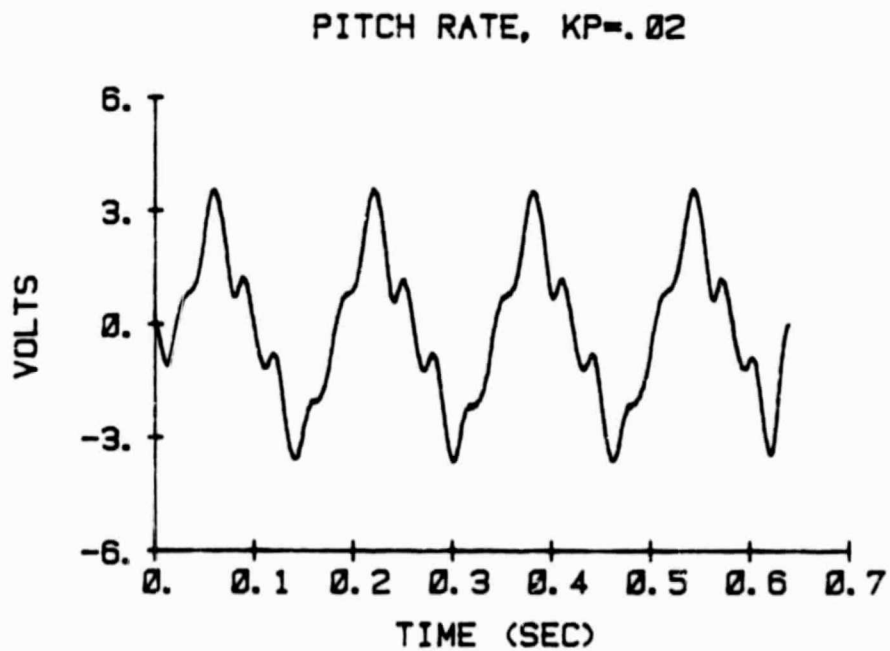
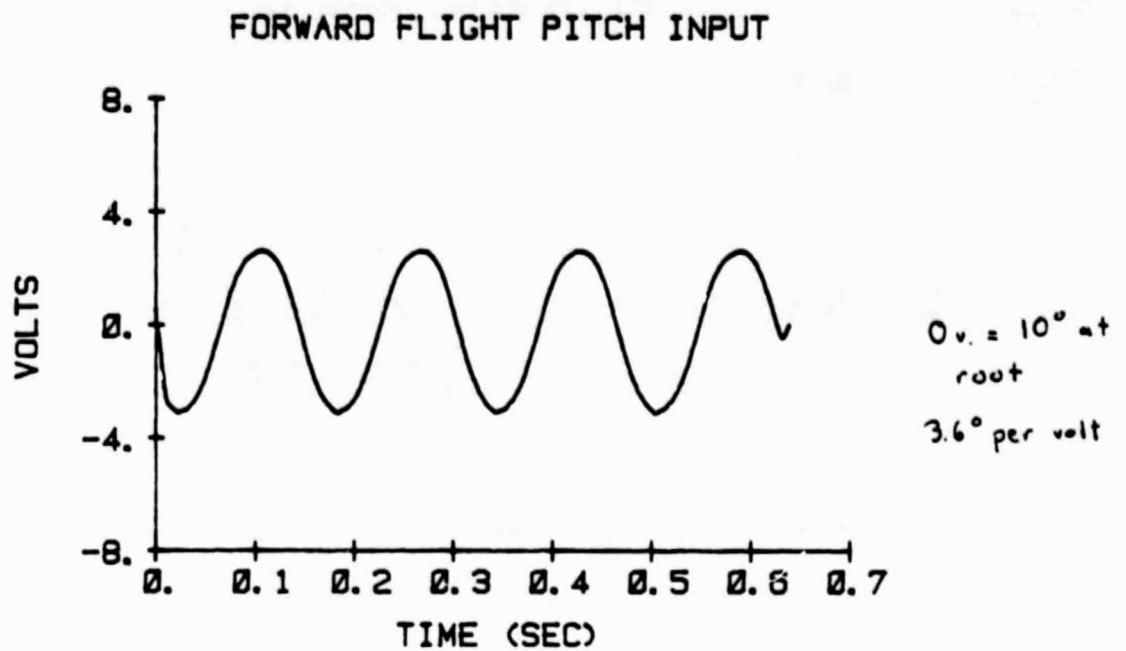


FIG. 33 Low Feedback, Mechanical Spring Test, $\Omega = 6.1$ Hz,
 $\mu = 0.33$

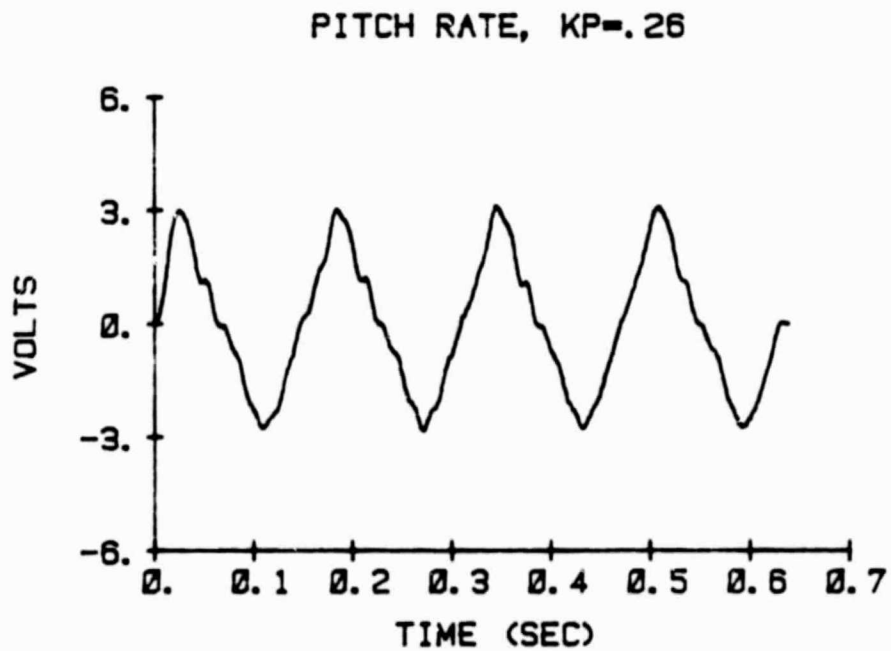
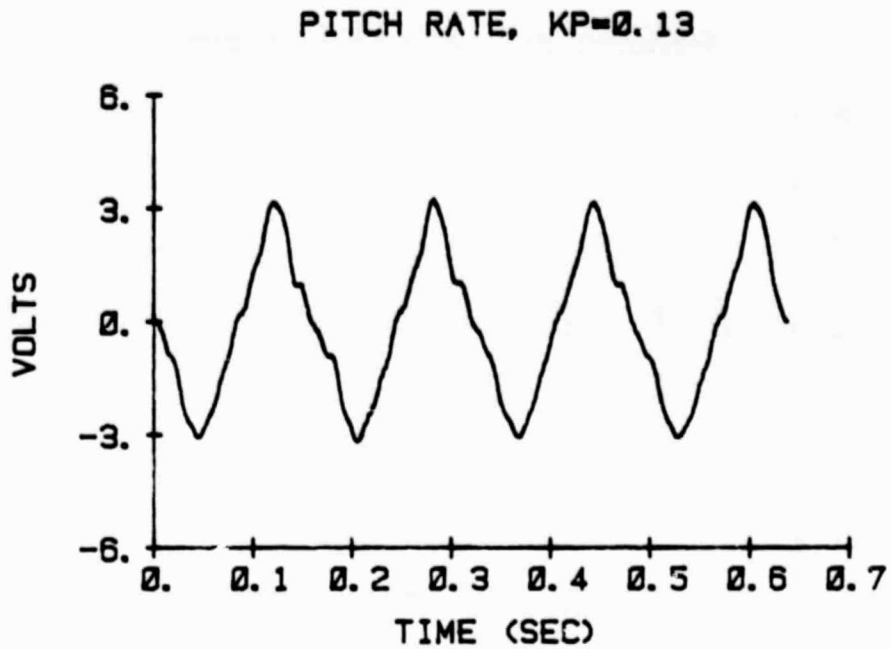
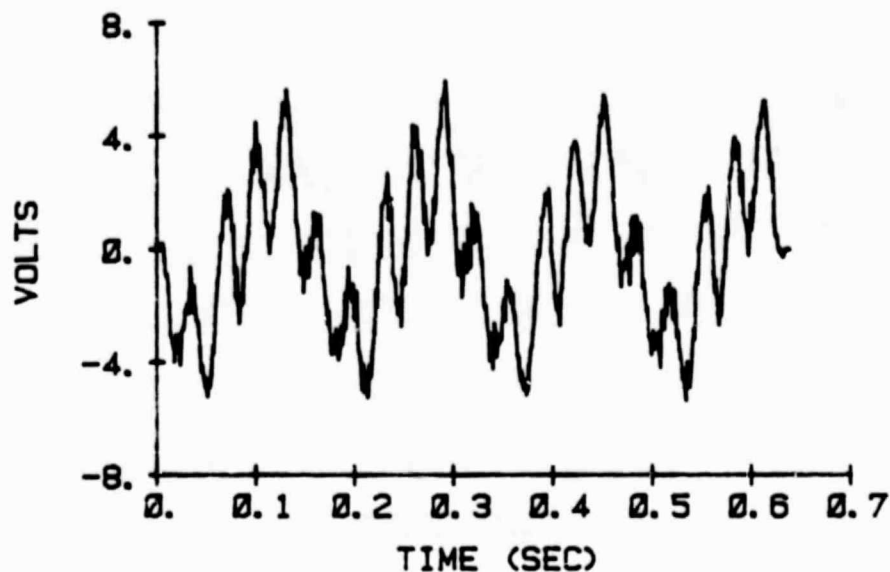


FIG. 34 Moderate and High Feedbacks, Mechanical Spring Test,
 $\Omega = 6.1 \text{ Hz}$, $\mu = 0.33$

PITCH ACCELERATION, $KP=.02$



FFT OF ACCELERATION, $KP=.02$

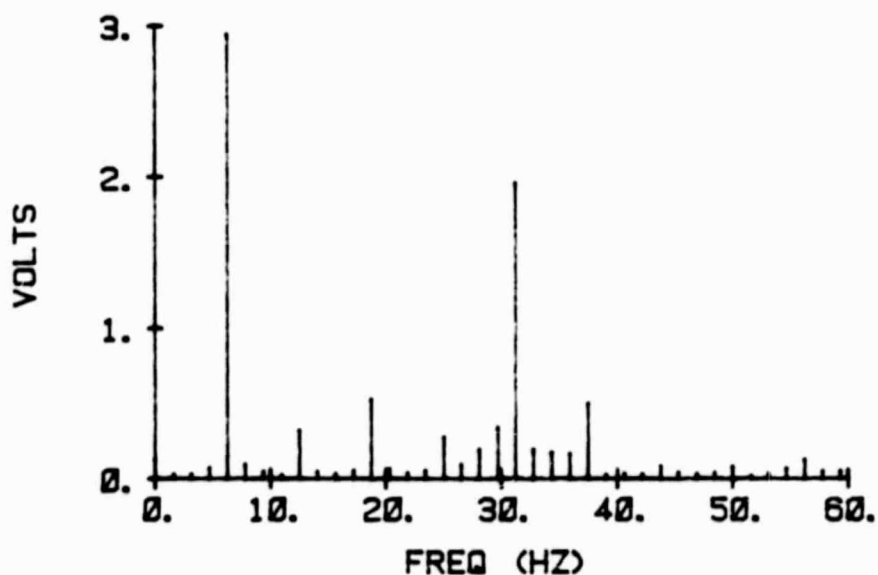


FIG. 35 Low Feedback Mechanical Spring Test, $\Omega = 6.1$ Hz,
 $\mu = 0.33$

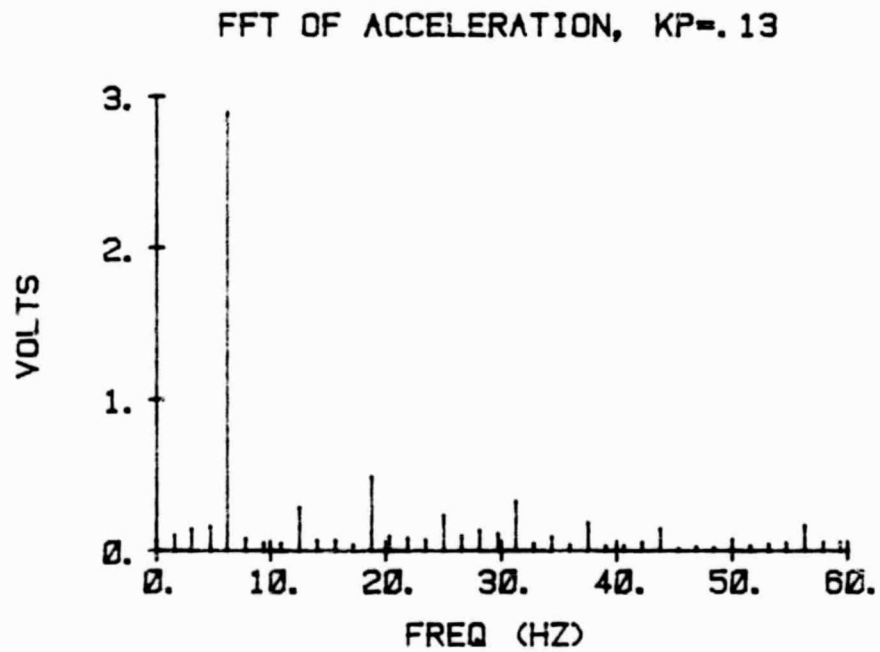
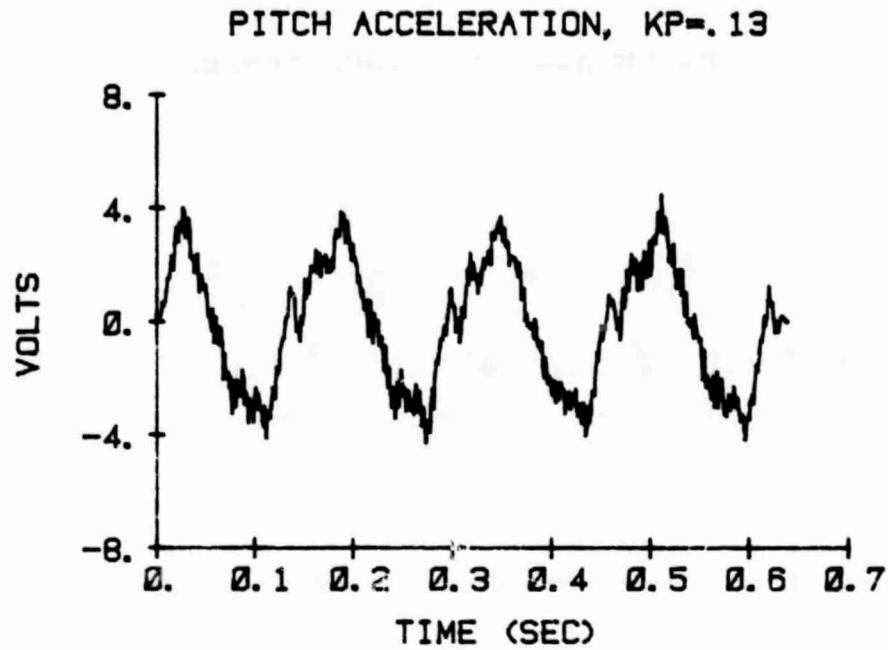
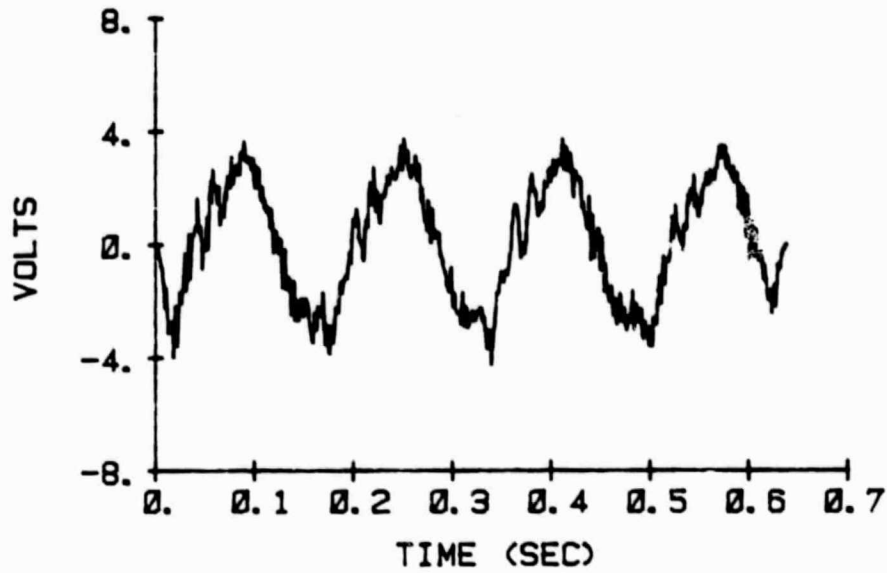


FIG. 36 Moderate Feedback Mechanical Spring Test, $\Omega = 6.1$ Hz,
 $\mu = 0.33$

PITCH ACCELERATION, $KP=.26$



FFT OF ACCELERATION, $KP=.26$

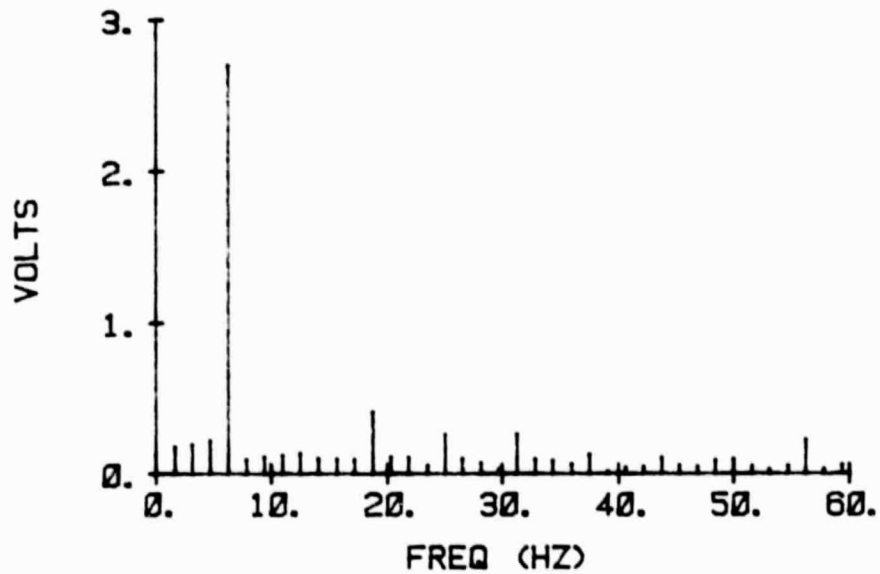


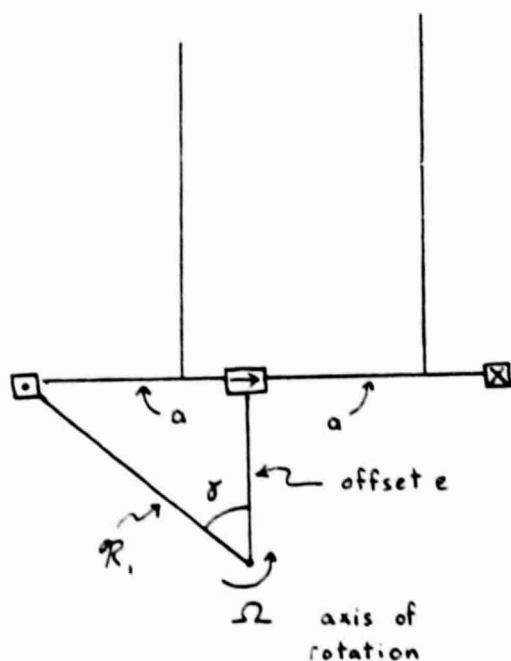
FIG. 37 High Feedback Mechanical Spring Test, $\Omega = 6.1$ Hz,
 $\mu = 0.33$

APPENDIX 1

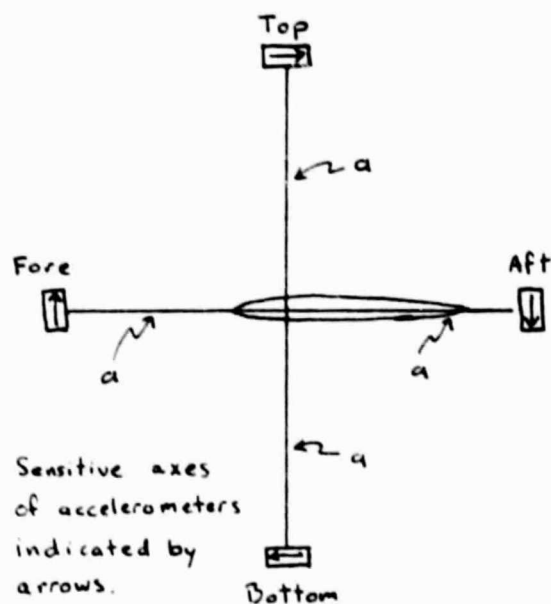
ACCELEROMETER PLACEMENT AND SIGNAL EXTRACTION

Consider four accelerometers to be rigidly attached to the root of a rotor blade, each a distance a from the pitch axis (.25c) as shown below:

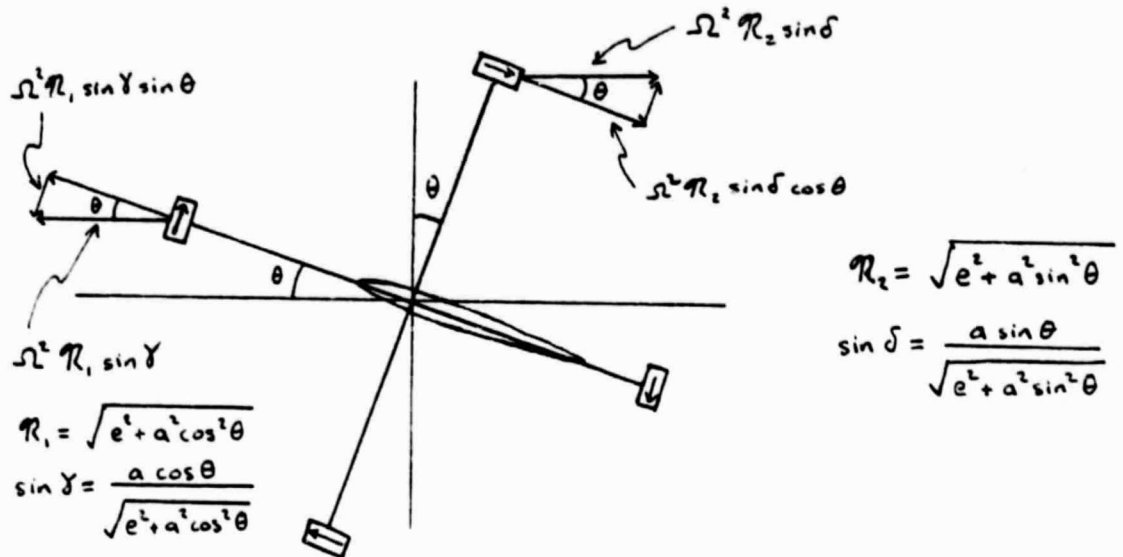
1 Top View



2 Side View



When the blade moves about its pitch axis, each accelerometer will produce a signal purely proportional to $a\ddot{\theta}$ if the chord of the blade is perpendicular to the axis of rotation (i.e. $\theta = 0$). However, if $\theta \neq 0$, the situation pictured below develops:



Fore accelerometer senses: $a\ddot{\theta} - \Omega^2 R_1 \sin \gamma \sin \theta =$

$$a\ddot{\theta} - \Omega^2 R_1 \left(\frac{a \cos \theta}{R_1} \right) \sin \theta = a\ddot{\theta} - \Omega^2 a \cos \theta \sin \theta$$

Top accelerometer senses: $a\ddot{\theta} + \Omega^2 R_2 \sin \delta \sin \theta =$

$$a\ddot{\theta} + \Omega^2 R_2 \left(\frac{a \sin \theta}{R_2} \right) \cos \theta = a\ddot{\theta} + \Omega^2 a \sin \theta \cos \theta$$

Sum Signals from Top and Fore accelerometers to yield $2a\ddot{\theta}$;
purely proportional to $\ddot{\theta}$.

Exactly the same result could be obtained by summing the signals
from the Aft and Bottom accelerometers.

Note that if the distances of the accelerometers from the pitching axis are not precisely equal the sum of the two signals will contain a component proportional both to θ and to the difference in the distances.

Appendix 2

DEVELOPMENT OF SYSTEM DYNAMIC EQUATIONS

For the case in which the servomotor shaft and the blade have a rigid connection, the motor can be described using the following equations of motion:

$$I L_a + I R + K_E \dot{\theta}_c = V \quad (A2.1)$$

$$-K_T I + J_T \ddot{\theta}_c + D \dot{\theta}_c = 0 \quad (A2.2)$$

where

- I = current through motor, amps
- V = voltage input to motor
- θ_c = angle of motor shaft, radians
- L_a = motor inductance = 1.09×10^{-2} ohm-sec
- R = motor resistance = 4.93 ohms
- K_T = torque sensitivity = .191 n-m/amp
- K_E = volts back EMF = 20 v/1000 rpm = .191 volt-sec
- D = motor viscous friction constant = 3.82×10^{-5} n-m-sec
- J_T = sum of motor, tachometer, linkage, and blade inertias = 8.35×10^{-5} kg-m²

The equations of motion can be reexpressed as

$$\begin{bmatrix} (sL/R + 1) & K_E/Rs \\ -K_T & J_T s^2 + Ds \end{bmatrix} \begin{bmatrix} I \\ \theta_c \end{bmatrix} = \begin{bmatrix} 1/R \\ 0 \end{bmatrix} [V] \quad (A2.3)$$

To find the transfer function $\dot{\theta}_c/I$, take the quotient of $\dot{\theta}_c/V$ and I/V .

$$\frac{\dot{\theta}_c}{V} = \frac{\begin{vmatrix} sL/R + 1 & 1/R \\ -K_T & 0 \end{vmatrix}}{\Delta(s)} = \frac{K_T/Rs}{\Delta(s)} \quad (A2.4)$$

$$\frac{I}{V} = \frac{\begin{vmatrix} 1/R & K_E/Rs \\ 0 & J_T s^2 + Ds \end{vmatrix}}{\Delta(s)} = \frac{1/Rs (J_T s + D)}{\Delta(s)} \quad (A2.5)$$

$\Delta(s)$ = system characteristic equation

So,

$$\frac{\dot{\theta}_c}{I} = \frac{K_T/Rs}{1/Rs (J_T s + D)} = \frac{K_T/D}{(1 + J_T/Ds)} = \frac{5000}{(s/457 + 1)}$$

This, along with the block diagram of Fig. 7, permits the derivation of Eq. 1 in the text, so long as the high frequency dynamics of the pitch flexure are neglected; if these dynamics are to be included, the closed loop transfer function for the pitch control system becomes, for $K_{\theta} = .05$, $K_{\theta} = .234$:

$$\frac{\theta_c}{V} = \frac{.298}{(1 - s/p_1)(1 - s/\bar{p}_1)(1 - s/p_2)(1 - s/\bar{p}_2)} \quad (A2.6)$$

$$p_1 = -182.7 + 416.0j$$

$$p_2 = -164.2 + 328.5j$$

Equation 6 allows the derivation of Eq. 2 in the text.

To include the effects of the mechanical torsional spring, the equations of motion of the blade/servo system become:

$$\dot{I} L_a + IR + K_{\theta} \theta_c = V \quad (A2.7)$$

$$-K_{\tau} I + J_{\tau} \ddot{\theta}_c + D \dot{\theta}_c + \frac{K_{\theta}}{2} \left(\frac{\theta_c}{2} - \theta \right) = 0 \quad (A2.8)$$

$$J_{\theta} \ddot{\theta} + K_{\theta} (\theta - \theta_c/2) = 0 \quad (A2.9)$$

Equation 9 is the blade/spring equation of motion

K_{NR} = non-rotating torsional spring constant of mechanical spring = 3.53 n-m/rad

J_B = inertia of blade, clamps, and counterweights
 = 9.31×10^{-5} kg-m²

J_T = inertia of motor, tachometer, and linkage
 = 8.11×10^{-5} kg-m²

Note the effects of the 2:1 reduction gear between the servo-motor shaft and the blade on Eqs. 8 and 9.

Equations 7, 8, and 9 can be reexpressed as

$$\begin{bmatrix} s\frac{L_0}{R} + 1 & K_E/R & 0 \\ -4K_T/K_{NR} & \frac{4J_T s^2 + 4D_T s + 1}{K_{NR}} & -2 \\ 0 & -1/2 & \frac{J_B s^2 + 1}{K_{NR}} \end{bmatrix} \begin{bmatrix} I \\ \theta_c \\ \theta \end{bmatrix} = \begin{bmatrix} 1/R \\ 0 \\ 0 \end{bmatrix} [V]$$

Using matrix manipulation methods similar to those used in the previous case, we obtain

$$\frac{\theta_c}{I} = \frac{K_T/D \left(\frac{J_B}{K_{NR}} s^2 + 1 \right)}{\frac{J_B J_T}{K_{NR} D} s^3 + \frac{J_B}{K_{NR}} s^2 + \left(\frac{J_B}{4D} + \frac{J_T}{D} \right) s + 1} \quad (A2.10)$$

$$= \frac{5000 \left(\frac{s^2}{(194.7)^2} + 1 \right)}{\left(\frac{s}{.366} + 1 \right) \left(1 - \frac{s}{p_3} \right) \left(1 - \frac{s}{\bar{p}_3} \right)}$$

$$p_3 = -.057 + 220.1j$$

Using this and the feedback gains $K_\theta = .528$ and $K_{\dot{\theta}} = .19$, the closed loop transfer function for the servo block in Fig. 12 becomes

$$\frac{\theta_c}{V} = \frac{.131 \left(\frac{s^2}{(194.7)^2} + 1 \right)}{\left(\frac{s}{1227.0} + 1 \right) \left(\frac{s}{160.6} + 1 \right) \left(1 - \frac{s}{p_4} \right) \left(1 - \frac{s}{\bar{p}_4} \right)} \quad (A2.11)$$

$$p_4 = -2.75 + 192.9j$$

Including the effects of blade and feedback dynamics as shown in Fig. 12 yields the open loop transfer function in the following form;

$$G_{ol} = \frac{.127 K_F s^3}{\left(\frac{s}{160.6} + 1\right) \left(\frac{s}{1227.0} + 1\right) \left(1 - \frac{s}{P_4}\right) \left(1 - \frac{s}{P_4}\right) \left(1 + \frac{s}{3.0}\right)^2} \quad (A2.12)$$

where K_F includes the gains of both the accelerometer block and the integrator block.

This open-loop transfer function was used to generate the root locus diagram in Fig. 13. Loop gain K_L in that diagram is equal to $.127 K_F$.

To model the effects of aerodynamic damping on the above results, a term $D_A \dot{\theta}$ can be introduced into the blade/servo equations of motion, Eqs. 7, 8, and 9. The new equations are, in Laplace-transformed form,

$$(s L_0/R + 1) I + (K_E/R) \theta_c = (1/R) V \quad (A2.13)$$

$$(-4K_T/K_{NR}) I + \left(4J_T/K_{NR} s^2 + \frac{4D}{K_{NR}} s + 1\right) \theta_c - 2\left(1 + \frac{D_A}{K_{NR}} s\right) \theta = 0 \quad (A2.14)$$

$$\left(-\frac{1}{2}\right) \theta_c + \left(\frac{J_B}{K_{NR}} s^2 + \frac{D_A}{K_{NR}} s + 1\right) \theta = 0 \quad (A2.15)$$

Again using straightforward applications of Cramer's Rule, these equations can be used to find $\dot{\theta}_c/I$:

$$\frac{\dot{\theta}_c}{I} = \frac{K_T/D \left(\frac{J_B}{K_{NR}} s^2 + \frac{D_A}{K_{NR}} s + 1 \right)}{\frac{J_B J_T}{D K_{NR}} s^3 + \left(\frac{J_T D_A}{D K_{NR}} + \frac{J_B}{K_{NR}} \right) s^2 + \left(\frac{J_T}{D} + \frac{J_B}{4D} + \frac{D_A}{K_{NR}} \right) s + 1} \quad (A2.16)$$

As noted in the text, the value of D_A changes with azimuth; a "worst-case" value for D_A , corresponding to $\zeta_{eff} \approx -0.1$ in the blade equation of motion (Eq. 15), might be $D_A = -3.6 \times 10^{-3}$ n-m-sec. Inserting this value in Eq. 16 yields

$$\frac{\dot{\theta}_c}{I} = \frac{5000 \left(\frac{s^2}{(194.7)^2} + \frac{2(-0.1)}{194.7} s + 1 \right)}{\left(\frac{s}{.36} + 1 \right) \left(1 - \frac{s}{p_5} \right) \left(1 - \frac{s}{\bar{p}_5} \right)} \quad (A2.17)$$

$$p_5 = +19.0 + 220.9j$$

For $K_\theta = .528$, $K_\theta^* = .19$, this leads to a closed loop transfer for the servomotor of

$$\frac{\theta_c}{V} = \frac{.131 \left(\frac{s^2}{194.7^2} + \frac{2(-0.1)}{194.7} s + 1 \right)}{\left(\frac{s}{160.0} + 1 \right) \left(\frac{s}{1207.1} + 1 \right) \left(1 - \frac{s}{p_6} \right) \left(1 - \frac{s}{\bar{p}_6} \right)} \quad (A2.18)$$

$$p_6 = +16.9 + 192.3j$$

while the open loop transfer function of the entire control system becomes

$$G_a = \frac{.127 K_F s^3}{\left(\frac{s}{1207.1} + 1 \right) \left(\frac{s}{160.0} + 1 \right) \left(1 - \frac{s}{p_6} \right) \left(1 - \frac{s}{\bar{p}_6} \right) \left(1 + \frac{s}{3.0} \right)^2} \quad (A2.19)$$

Using Eq. 19, the root locus diagram for the system including large negative aerodynamic damping was generated in Fig. 13; though this model of the effects of dynamic stall on the blade is clearly an approximation (since, in reality, stall effects have a highly complex dependence on $\dot{\theta}$, $\ddot{\theta}$, and other variables), the above example shows that the system proposed herein can be expected to perform adequately even under very adverse conditions at constant negative damping. On a real rotor, of course, the blade is exposed to effective negative damping only for a small fraction of each revolution.

Note also that the above analyses have been performed under the assumption that the effects of rotor rotation on the torsional spring constant K_{NR} were negligible. In reality

$$K_R = K_{NR} + J_B \Omega^2$$

A typical value of Ω in these tests was 6.7 Hz, which yields

$$K_R = 3.52 + (9.31 \times 10^{-5}) ((6.7)(6.28))^2 = 3.69$$

The difference between K_R and K_{NR} was deemed to in fact be negligible for present purposes, especially since the change effected due to rotation in the spring natural frequency was less than the resolution of the Fourier transform routine used in data analysis.